A Certification-Driven Platform for Multidisciplinary Design Space Exploration in Airframe Early Preliminary Design

Darshan Sarojini*, Jiacheng Xie†, Yu Cai‡, Jason A. Corman§, and Dimitri N. Mavris¶
Aerospace Systems Design Laboratory, School of Aerospace Engineering
Georgia Institute of Technology, Atlanta, Georgia, 30332

Following the conceptual phase of aircraft design, sizing and performance estimations shift from historical-based empirical equations to physics-based simulations. The initial aircraft configuration is refined with a larger number of objectives and requirements, and certification regulations play a critical role in defining these. Analysis tools in the early phases of preliminary design have an important trade-off between accuracy, complexity, and computational efficiency. A number of analysis frameworks currently exist with varying levels of fidelity, multidisciplinary coupling, and limitations in the number of disciplines, degrees of freedom, and requirements they are able to implement. To enable efficient design space exploration (DSE), this paper proposes an integrated preliminary design framework that couples aerodynamics, structures, subsystems, aircraft performance, flight dynamics, and certification testing at varying levels of fidelity. This framework serves as a numerical testbed that can be used to explore the aircraft configuration and disciplinary design spaces, strength of disciplinary couplings, and propagate disciplinary uncertainties across the entire aircraft system. The framework is demonstrated using the horizontal tail of a large twin-aisle aircraft as a test case.

I. Introduction

Aircraft design is multi-disciplinary, multi-objective and multi-stage process. The design process in its early phases involves considerations from aerodynamics, structures, performance, stability and control, propulsion, manufacturing, and cost. These disciplines may lead to conflicting objectives involving numerous trade-offs and decisions. For example, one trade-off is between safety, performance and cost. We can mitigate structural failure by reinforcing every component with more material. However, this would cause a significant weight penalty, which affects performance and cost.

Although an aircraft design process can be broken up into any number of stages dependent on an organization's particular set of milestones, it has generically been characterized in many publications within three phases: conceptual, preliminary and detailed design. At the conceptual phase, an initial sizing is performed based on point and mission requirements, generally specified in a request for proposal (RFP) or concept of operations (CONOPS). These provide a rough estimate of the aircraft aerodynamic, propulsion, weight, and performance characteristics. A number of tools has been implemented for the conceptual design phase, including FLOPS [1], EDS [2], SUAVE [3], MARILib [4], and TASOPT [5], which are widely parametric and execute quickly to investigate these trade-offs. Furthermore, rapid execution of these tools also enables potentially burdensome uncertainty quantification techniques for metrics of interest. Following conceptual design, the initial sizing is refined with a larger number of objectives and requirements.

Moving beyond simplified conceptual design tools, disciplinary models and their multidisciplinary integration tend to shift toward codes at multiple levels of fidelity that are tightly coupled. Cavagna [6] developed a tool named NeoCASS to perform structural sizing and optimization considering aeroelasticity. The toolkit provides the flexibility to use varying levels of fidelity in the structural and aerodynamic disciplines, and uses a combination of physics-based method and semi-empirical regressions to perform sizing. Altus and Kroo [7] represented the wing as a box beam and performed multi-disciplinary design optimization using the Optimizer-Based Decomposition (OBD) architecture, coupling aerodynamics and structural analysis. Weights are computed empirically here. Piperni et al. [8–10] describe an MDO environment named VADOR. Aerodynamics is considered through the use of CFD. Skin, cap, stringers and spars are considered, and wing weight is estimated using plate theory. Sizing of the structure is also done using plate

*Ph.D. Candidate, Senior Graduate Researcher, ASDL, School of Aerospace Engineering, Georgia Tech, AIAA Student Member
†Ph.D. Student, Senior Graduate Researcher, ASDL, School of Aerospace Engineering, Georgia Tech, AIAA Student Member
‡Ph.D. Student, Senior Graduate Researcher, ASDL, School of Aerospace Engineering, Georgia Tech, AIAA Student Member
§Research Engineer II, ASDL, School of Aerospace Engineering, Georgia Tech, AIAA Member
¶S.P. Langley Distinguished Regents Professor and Director of ASDL, Georgia Tech, AIAA Fellow

theory. Loads are obtained from aeroelastic analysis, where a stickmodel is used. The stickmodel is extracted from the full FEM. Asymmetric Subspace Optimization (ASO) MDO architecture is used. Martins et al. developed a low-fidelity aerostructural MDO environment named OpenAeroStruct [11]. OpenAeroStruct uses a panel method to obtain the loads. The structure is modelled as a circular beam using Euler-Bernoulli beam theory. Static aeroelastic considerations are used while performing optimization. Martins et al. also developed a MDO tool named MACH [12, 13](MDO of Aircraft Configurations with High fidelity). MACH uses a CFD solver, ADFlow, for aerodynamics. The structure is represented as thin-walled shells and solved using TACS [14](Toolkit for the Analysis of Composite Structures). MACH allows for efficient high-fidelity aerostructural optimization of aerodynamic and structural design variables.

In the preceding frameworks for preliminary design and their associated research applications, there are a few areas of potential improvement. First, the certification requirements that are used to set up load cases and flight conditions are typically limited to simplified static maneuvers defined in 14 CFR Part-25 Subpart-C. Additionally, the higher fidelity simulation capabilities that are leveraged in some frameworks are appropriate in scenarios in which higher accuracy is more imperative; however, investigating significant configuration changes and large design spaces are computationally intractable. Finally, representation of subsystems and their impacts on performance are limited as well. Therefore, the main motivation in the development of this research is to create a framework that can: 1] move into the dynamic realm of flight and structure certification regulations (14 CFR Part-25 Subparts B and C), 2] explore a large multidisciplinary design space while maintaining as many configuration degrees of freedom as possible from the conceptual design phase, and 3] consider subsystem sizing and effects in overall performance predictions.

In this work, we develop a modular framework that can be used to size the airframe at the early preliminary design phase, with an emphasis on certification requirements driving the sizing process. We use low-order models which implement fundamental physics of structures, aerodynamics, flight performance, stability and control. The vehicle-level impact such as mass, drag, secondary power extraction is also considered for sub-systems. The low-order models are computationally fast and hence, amenable to design-space exploration and uncertainty quantification.

The remainder of this paper is organized as follows: Section II describes disciplinary analyses and associated computational tools applied in the framework. Section III defines the test case of designing the horizontal tail (HT) for a large twin-aisle aircraft (LTA) using the integrated framework. Section IV presents the results of design space exploration and multidisciplinary optimization of the test case.

II. Computational Techniques

Figure 1 presents the notional extended design structure matrix [15] for the proposed framework, where $\vec{x}$ is the design variable vector, S_{ref} the reference wing area, b_{ref} the reference wing semi-span, c_{ref} the reference wing chord, $\vec{r}_{comp,i}$ the location of component i, ΔC_D the impact of subsystems on the aircraft drag coefficient, $\dot{m}_{bx}$ the bleed extraction, and P_{spx} the shaft power extraction. Each disciplinary analysis module is briefly described in the following subsections.

A. Geometry Manager

A geometry definition is needed for aerodynamics, structures and mass properties of the aircraft. The geometry manager should allow for the following:

1) **Aerodynamics Definition**: Requires an outer mold line (OML) to define the surface in contact with airflow. The definition must be parametric to allow for automated deviations of high-level design variables, such as wing area, aspect ratio (AR), and sweep.
2) **Structures Definition**: A parametric tool should be capable of defining various structural layouts and creating aircraft structural components such as spars, skin and ribs. Automated meshing of these various configurations is also paramount to the success of batch-processing designs of experiments to explore the design space.
3) **Structural Mass Properties Definition**: For a given structure, material is assigned to each component. Material and geometry definition together allows for the computation of mass properties.
4) **Subsystem Layout**: For a given subsystem architecture, the logical connectivity between propulsion system, secondary power generation and distribution subsystems (PGDS), and power consuming subsystems (PCS) are established and mapped to physical connectivity based on OML.

The geometry manager used in this work is facilitated through the RADE toolkit [16], developed at the Aerospace Systems Design Laboratory (ASDL). RADE contains a module for parametric variation of a baseline OML through the OpenVSP API, where aerodynamic shape variables such as span, sweep, chord, area, AR, twist, among others can be defined. An example relevant to the application presented in this paper is shown in Fig. 2a, where a baseline horizontal

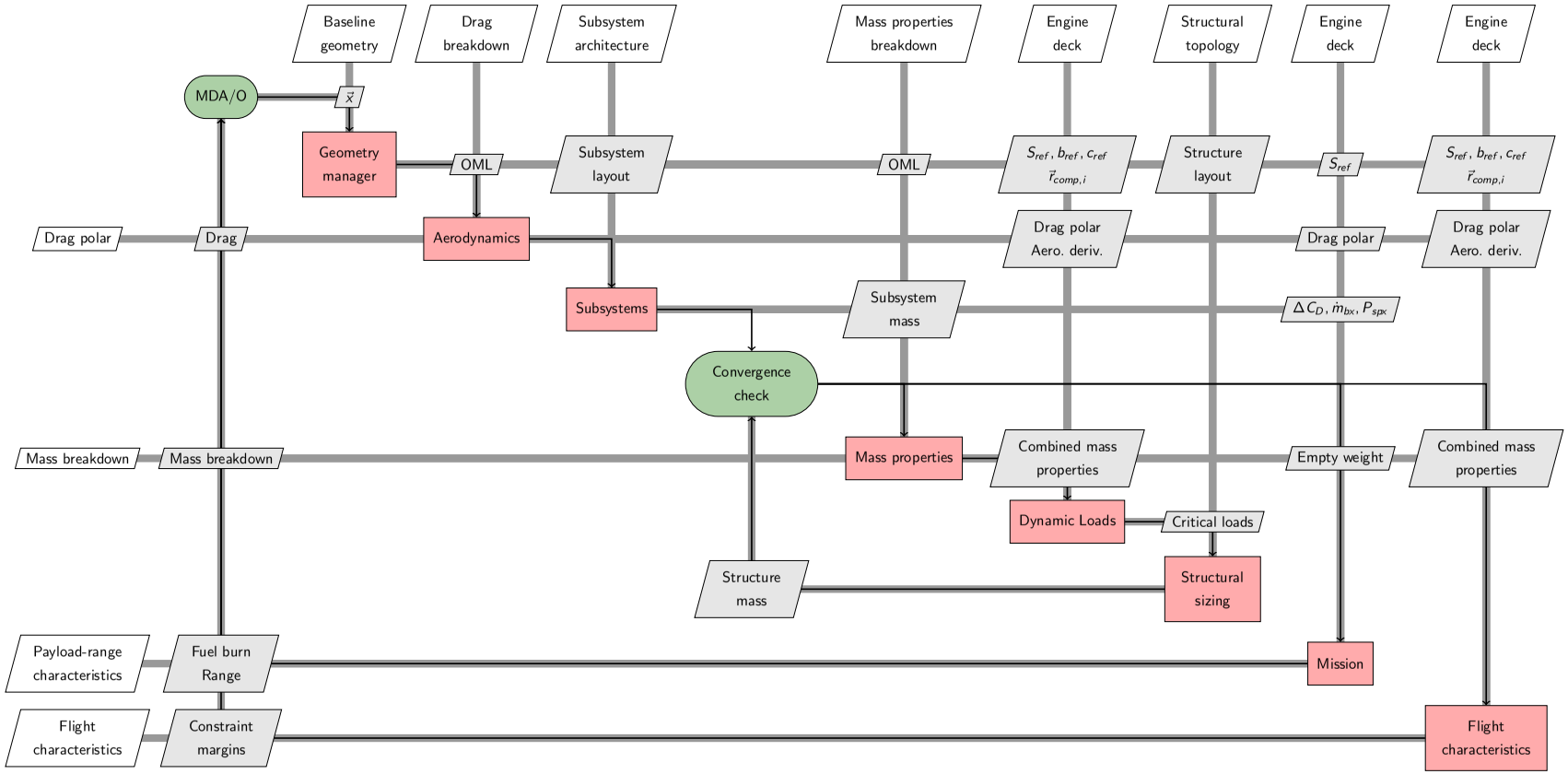

Fig. 1 Notional design structure matrix for the proposed framework

tail (gold) was changed to a planform with a larger sweep angle, higher aspect ratio, and smaller taper ratio.

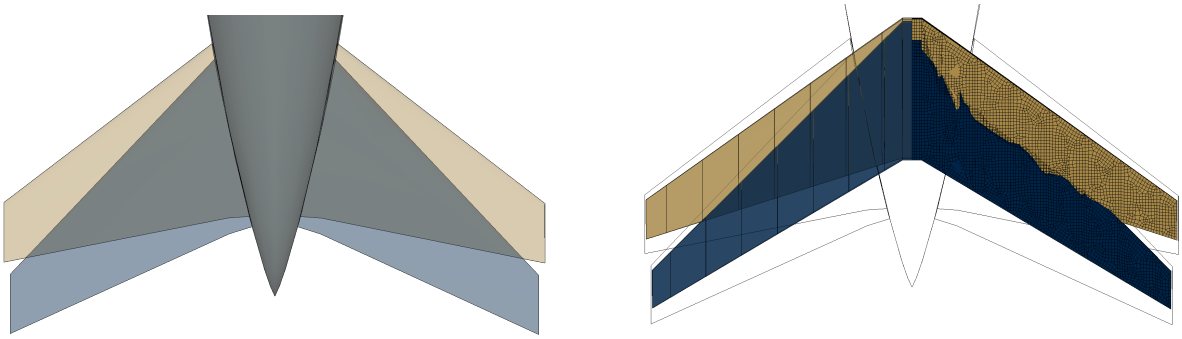

(a) Outer mold line **(b) Structural geometry and mesh**

Fig. 2 Parametric features of the geometry pre-processer on the HT

Once the OML is defined, RADE has an automated capability to create a structural topology within the bounds of the OML. This is also a parametric implementation, and RADE has a library of various topological categories, each with its own set of parameters. Figure 2b shows a simple two spar wingbox for the horizontal tail (HT) in which variation of the front and rear spar locations, rib spacing, and rib orientation can be defined. The RADE structural geometry module then spar, rib, and skin parts into an assembly hierarchy, in which various definitions can be made for the discretization of surfaces to set up material and sectional properties. A structural mesh can also be created automatically with definitions supplied by the user, including desired mesh size, growth rates, curvature rules, and element types. Example meshes for both configurations can be seen plotted on top of each other in the right side portion of the HT in Fig. 2b, but these capabilities are not limited to a single component or section of the aircraft. Figure 3 shows structural geometry layout and mesh for the wing, horizontal tail, and vertical tail within a fused representation of the OML for the common research model (CRM).

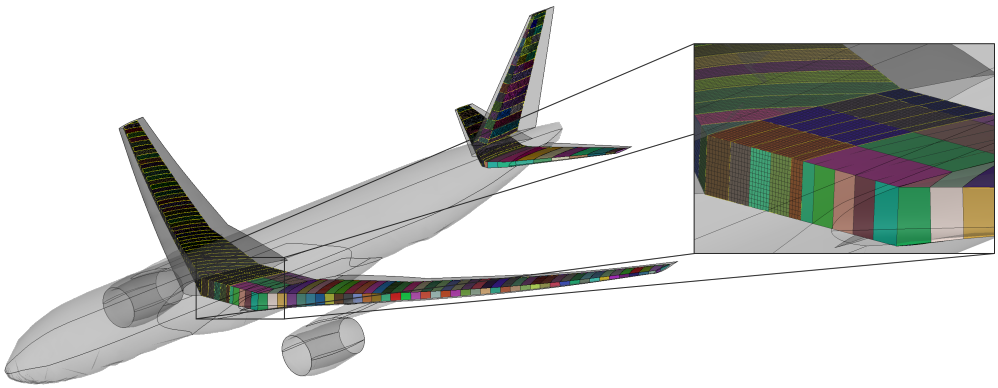

Fig. 3 Parametric mesh generation capability: geometry and mesh of mesh of wing and empennage of the CRM

When using a shell-like surface structure model like these figures depict, a number of options exist for setting up properties of the structure. For each component panel, the mass of the structure is computed as

$$m_i = S_i t_i \rho_i \tag{1}$$

where S_i is the area of each mid-surface, t_i is an effective thickness, and ρ_i the effective density of the material of the component panel. An effective thickness and density is used in this definition to allow for the use of "smeared" structural properties in which stiffener components and other non-structural mass elements can be used to tune the weight and stiffness of the think-wall shell implementation.

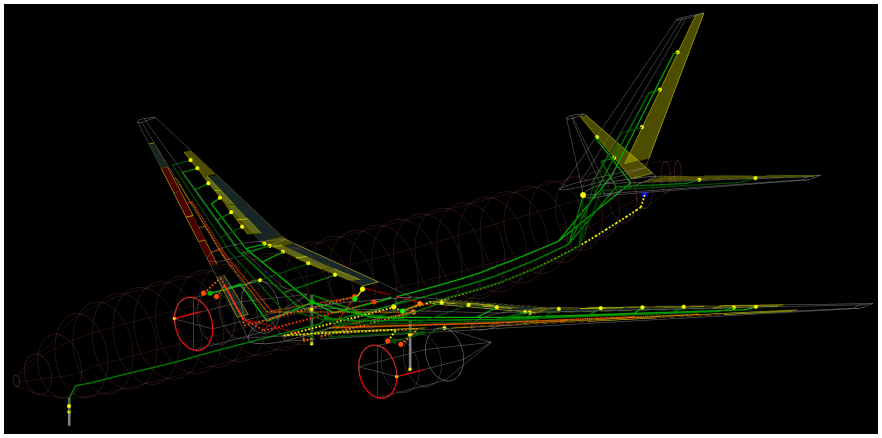

Fig. 4 Parametric layout for secondary power generation, distribution, and consuming subsystem architecture on tube-and-wing transport

Given a subsystem architecture, the logical connectivity between prime movers, power sources, power systems, power distribution elements, and power consumers are first established using an architecting algorithm [17]. The geometry manager then maps the logical connectivity to physical layout in the aircraft based on OML and key component locations, as shown in Fig. 4.

B. Aerodynamics

The role of an aerodynamic analysis is to approximate the pressure and shear stress distribution based on the aircraft geometry, as well as to enable the computation of the lift, drag, and stability and control derivatives needed for performance and flight dynamics evaluations. The choice of aerodynamic analysis method depends on the trade-off between accuracy and computational cost. In early preliminary design, because the design space exploration requires the evaluation for a large number of design candidates, the computational cost associated with the intermediate disciplinary analyses cannot be large. High-fidelity aerodynamic analysis methods such as RANS CFD and Euler CFD, although theoretically more accurate than the methods with simplified assumptions, are traditionally too expensive to evaluate a large number of design candidates without the support of high performance computing. The computational cost is especially exacerbated when one single design candidate needs multiple aerodynamic evaluations at a series flight conditions. In order to rapidly capture the aircraft aerodynamic characteristics while maintaining acceptable level of accuracy, this paper uses semi-empirical drag build-up method for the aircraft drag approximation and vortex lattice method for the calculation of stability and control derivatives.

Semi-empirical drag build-up method is a rapid drag evaluation method based on the Boundary Layer Theory and form factors. Because the method is corrected by historical data using statistical approach, it is able to capture the main effect from different drag sources including skin friction drag, pressure drag, induced drag, non-isentropic drag, and interference drag, etc. In the design loop, the drag build-up method is performed by the Flight Optimization Systems (FLOPS) developed from NASA [18].

Vortex lattice method (VLM) is low-fidelity method for the pressure field approximation using linearized potential flow. In the VLM, the lifting surfaces are model as discretized vortex panels following Biot-Savart Law and Kutta-Joukwski Theory, while the non-lifting bodies are model as sources/sinks or doublets to enforce the non-penetrating condition. The compressiblilty effect can be captured by incorporating the VLM with the Gorthert's Rule. Due to its nature of linearization, the VLM is able to quickly compute the stability and control derivatives. In the design loop, the vortex lattice method is executed by the open-source software AVL [19]. The input aircraft model used by AVL is parametrically generated by the Geometry Manager, as shown in Fig. 5.

C. Mass Properties

The mass properties analysis computes the weight, center of gravity (CG), and moments of inertia for the entire aircraft. The analysis involves two levels. The first level gives the initial approximation of aircraft gross weight, CG location, and moments of inertia to start the structure and subsystem sizing loop. In this level, the aircraft component

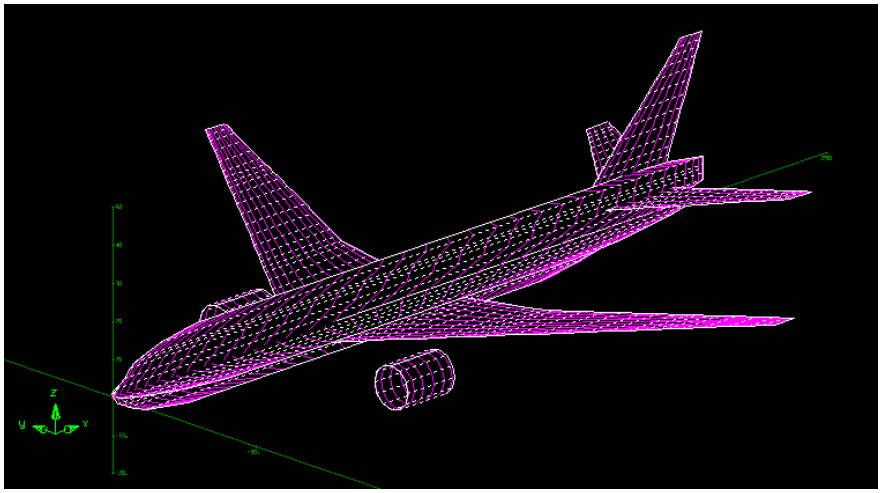

Fig. 5 Notional aircraft AVL model generated by Geometry Manager

weight is approximated by the statistical method using FLOPS [20] and the fuel weight is assumed given by aircraft conceptual sizing. The CG location is approximated based on the locations and weights of components. The moments of inertia are initially approximated by the Roskam's empirical method [21] which is based on the historical data of non-dimensional radii of gyrations. These initial mass properties approximations are sent to the analyses of dynamic load, structural sizing, and subsystems to size the aircraft structures and subsystems as described in following subsections.

The second-level analysis re-computes the aircraft mass properties based on the results from structural and subsystems sizing. The weight, center of gravity, and moments of inertia about its own CG of each structural component and each subsystem are updated from structural and subsystems sizing and tabulated as shown in Table. 1. The mass properties of the aircraft can then be recomputed using parallel and perpendicular axis theorems. Once the new aircraft-level mass properties are updated, they are sent back to structural and subsystems sizing. The analysis iterates between the structural and subsystems sizing and the mass properties analysis until the convergence in aircraft-level mass properties.

Table 1 Mass properties of each component about its own CG

Component	Weight	CG Location			Moments of Inertia					
		x_{oc}	y_{oc}	z_{oc}	I_{xx}	I_{yy}	I_{zz}	I_{xy}	I_{yz}	I_{zx}
1	...	.	.	.	.	.	.	.	.	.
...	...	.	.	.	.	.	.	.	.	.
n	...	.	.	.	.	.	.	.	.	.

D. Subsystems

This module concerns the aircraft equipment systems which consume secondary (non-propulsive) power to perform tasks essential to vehicle performance, safety, controllability, and passenger comfort. The subsystem analysis includes physics-based sizing of hydraulic, pneumatic, electric, and mechanical power generation and distribution subsystems and secondary power consuming subsystems based on vehicle geometry and critical operating condition(s) of individual subsystems. It then determines the mass, drag increment, and secondary power requirements of each subsystem, which are propagated back to vehicle-level mass properties analysis and mission analysis. Modules from the Integrated Subsystems Sizing and Architecture Assessment Capability (ISSAAC) [22, 23] are used in this work for subsystem analysis.

E. Dynamic Loads

The sizing of many structural components on an aircraft are typically driven by gust and dynamic maneuvers defined in Title 14 of the Code of Federal Regulations (14 CFR) Part-25 Subpart-C [24]. Maneuvers such as §25.331(c)(2),

commonly known as the *Checked Pitch Maneuver*, and §25.351, commonly referred to as the *Rudder Kick Maneuver* provide critical loads which size the horizontal tail and vertical tail respectively. Calculating critical loads is a multidisciplinary process that entails simulating the aircraft dynamics corresponding to the prescribed FAR maneuver for different flight conditions within the flight envelope and identifying the most severe loads.

A framework named Dynamic Environment for Loads Prediction and Handling Investigation (DELPHI) is under development at ASDL following prior work in [25–27]. An aircraft in DELPHI is defined by 1) mass properties (Section A), 2) aerodynamic characteristics (Section B) which describe the total forces and moments at a reference point as a function of aircraft states and control surface deflections, and 3) propulsive performance (engine deck) which define the propulsive loads at the reference point as a function of altitude, Mach number and throttle. Any desired maneuver can be input as a pilot command to simulate the actions a pilot would perform on a flight test. The framework integrates the *rigid-body* 6 DoF equations of motion forward in time to obtain a time history of aircraft states and control surface deflections.

The time history can then be used to obtain the external loads acting on the lifting surface. The proposed method involves dividing the lifting surface into sections, or "strips", with known aerodynamic characteristics and mass properties and then calculating the forces and moments that develop on each strip at each time step. Finally, the most severe loads are found from the time history of loads for each flight condition. A high-level flowchart of this process is shown in Figure 6.

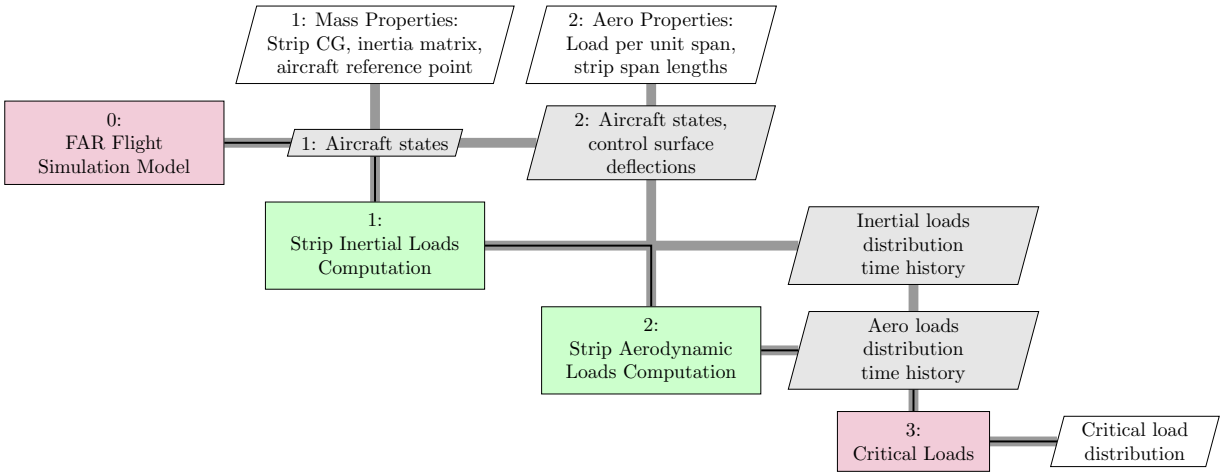

Fig. 6 Structural loads analysis flowchart

F. Structural Analysis and Sizing

The critical loads obtained by performing dynamic maneuvers (Section E) are used to size the structural components. In addition to externally applied loads, inertial loads associated with components and subsystems such as engines, control surfaces, actuators, hydraulic lines, etc. are implemented through concentrated masses. Figure 7 shows a structural layout for the HT with two concentrated masses for the two actuators of the elevator. The elevator structure itself is treated as a concentrated mass attached to the rear spar, and therefore its stiffness in the system is neglected. Thus, the mass of the subsystems (Section D) are accounted for in structural sizing.

The transfer of aerodynamic loads to the structure is performed through integration of surface pressures to reference points along the span of a wing-like component. A module in RADE [16, 28] estimates the elastic axis and sets these reference points at the intersection of this line with rib components. The forces and moments associated with each reference point are then distributed to the structure via rigid body elements at key intersecting nodes between the rib and skin. RADE also provides a module to translate data required for structural analysis and sizing to either Nastran or Hypersizer, execute the code, and obtain responses of interest. Along with stress, strain, and deflection distributions calculated in Nastran, potential component-based outputs from HyperSizer include: optimal sectional dimensions (skin thickness, stiffener height, etc.), margins of safety, critical load case, critical failure mode (categorization), and critical failure method (failure equation).

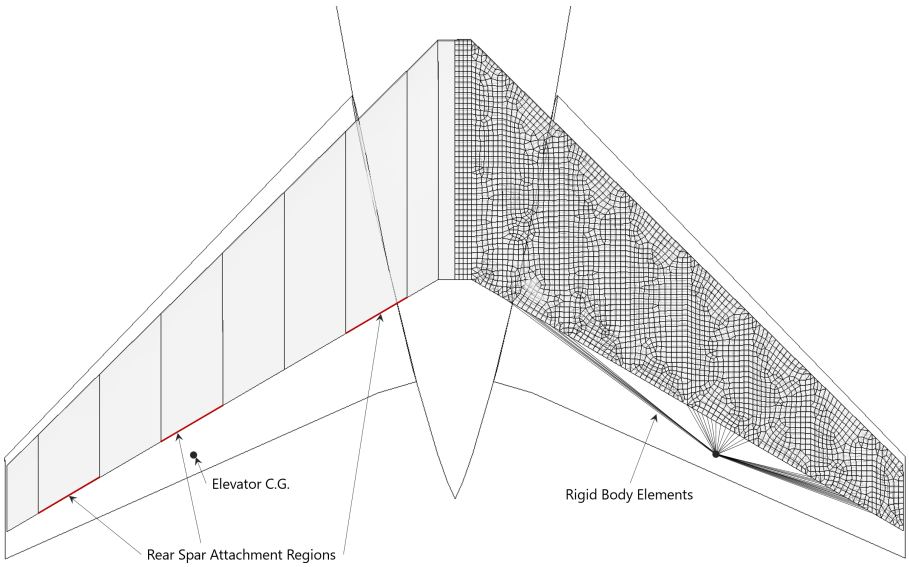

Fig. 7 Subsystems treated as concentrated masses and attached to the structure via rigid body elements

G. Mission Analysis

The mission analysis is performed to evaluate the candidate's range capability as part of design requirement verification, and to assess the candidate's mission performance such as fuel burn for specific mission(s). A generic mission profile for commercial transport is used in this work as shown in Fig. 8. The step cruise at fixed Mach number is assumed at altitudes between 31 000 ft and the service ceiling with an increment of 4000 ft. The initial cruise altitude is selected to maximize the specific air range at the top of climb.

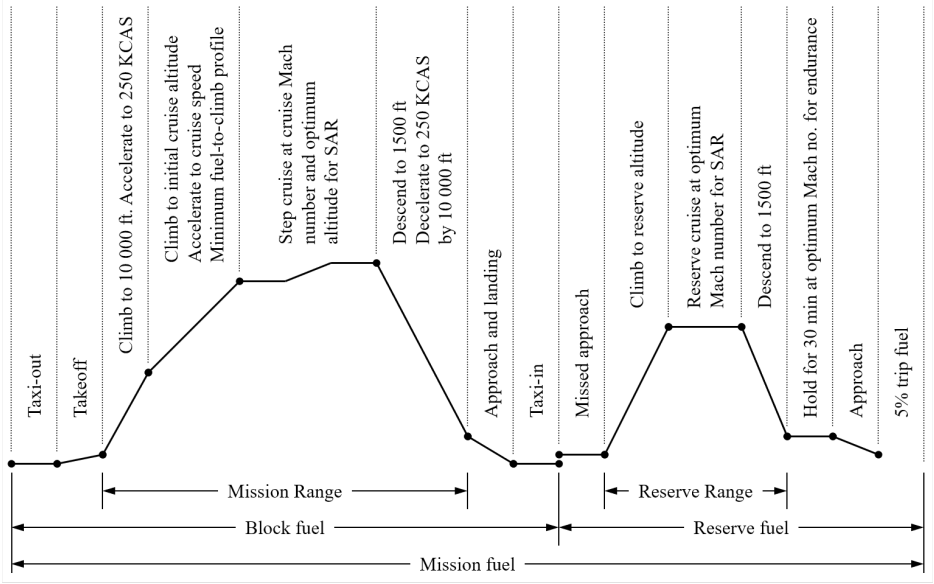

Fig. 8 Generic mission profile for commercial aircraft

Required inputs to the mission analysis module include the vehicle operating empty weight, payload weight, engine deck, and drag polar. Depending on type of analysis, mission range may be input to solve for ramp weight, or vice versa. The Aircraft Sizing and Off-Design Mission Analysis Tool [29] is selected for mission analysis. In this framework, the mission analysis is performed twice:

1) The baseline vehicle design gross weight is input as the ramp weight. The maximum range at design payload is

calculated as a constraint function to check against the requirement of design range.

2) An off-design mission with shorter range is selected as the input mission range. The corresponding ramp weight and mission fuel weight are calculated, the latter of which is used as an objective function.

When evaluating the block fuel consumption, an off-design mission is used in this evaluation, since the design range requirement may be violated for certain candidates, and the fuel consumption of a properly selected off-design mission can better reflect the direct operating cost for operators. The selection of the off-design mission is to be discussed along with the objective functions in Sec. III-C.

H. Flight Characteristics

The flight characteristics analysis is to evaluate the aircraft point mission performance and flight dynamics. In 14-CFR Part-25 Subpart-B [24], a series of performance and flight dynamics rules are specified to ensure the aircraft's flight safety and handling quality. To show the compliance with respect to these rules, the aircraft needs to conduct the flight tests following the procedures described in regulations and associated Advisory Circular [30]. In order to promote a viable design in terms of flight characteristics and reduce the time and cost spent on type certification stage, it is necessary to incorporate these certification requirements into early design stage. Because most of these rules requires the dynamic response of aircraft, the point-mass based method used in most of performance analyses is inadequate. Instead, the six degree-of-freedom flight dynamic simulation is needed.

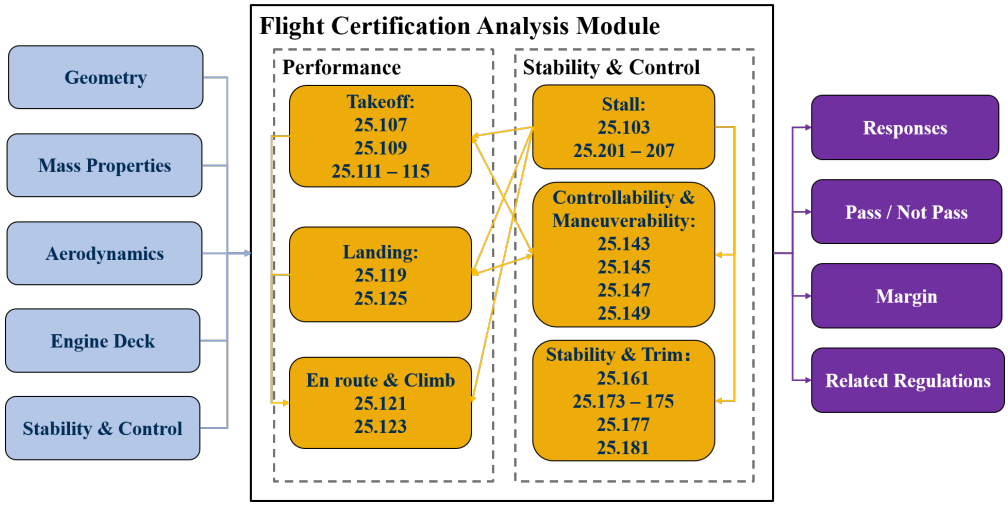

Fig. 9 Structure of Flight Certification Analysis Module [31]

To capture the flight characteristics design constraints posed by certification regulations, in this paper, the flight characteristics evaluation is performed by the Flight Certification Analysis Module [31]. The Flight Certification Analysis Module is an analysis tool developed in ASDL used to check aircraft performance and flight characteristic against the certification rules in 14-CFR Part-25 Subpart-B in early design phases. In the Certification Module, each Subpart-B regulation that defines explicit metrics or constraints is transformed into a quantitative constraint function in MATLAB. The general structure of the Certification Module is shown in Fig. 9. Six components are contained in the module: takeoff, landing, climb, stability, controllability, and stall. Each component contains the MATLAB functions of relevant regulations. The details about modelling of certification rules are documented in Ref. [31]. The input of the module is an aircraft representative model which includes the design information of aircraft geometry, mass properties of the whole aircraft, engine deck, and the drag polar and stability & control derivatives at takeoff, cruise, and landing configurations. Once the aircraft model is input to the module, the module will automatically check whether the current design satisfies the certification constraints following the flight test procedures described in regulations and the Advisory Circular. The checking process is enabled by a flight dynamic simulator established inside the Certification Module. The simulator is developed based on 6-DoF equations of motion with small-disturbance assumption. With the Total Energy Control System (TECS) integrated in the simulator, it is also able to perform closed-loop control for takeoff and landing simulation. The output from each regulation check includes the dynamic responses of current design, the compliance status, the margin with respect to the constraints defined in the regulation, as well as the cross-referenced regulations.

III. Test Case Formulation

To demonstrate this method, this paper scope to a case which incorporates all the disciplines being considered, but is not overly complicated. As the test case, a design space exploration and multi-objective, multi-disciplinary optimization for the preliminary horizontal tail (HT) design of a large twin-aisle aircraft (LTA) is performed.

A. Baseline Aircraft

The baseline aircraft selected for the test case is a 300-pax LTA model calibrated based on the open-source NASA Common Research Model (CRM). The vehicle was sized based on the mission profile of B777-200ER aircraft [32] and the aircraft model was established through conceptual design analysis using EDS, which generates an empty weight breakdown, drag build-up, and engine deck [33]. The key geometry and performance specifications of the baseline aircraft are shown in Table 5 of Appendix A.

1. Flight and CG Envelope

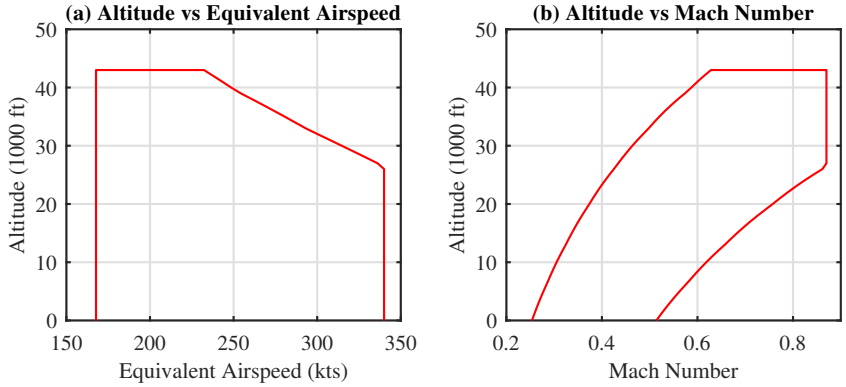

Fig. 10 Flight envelope in clean configuration

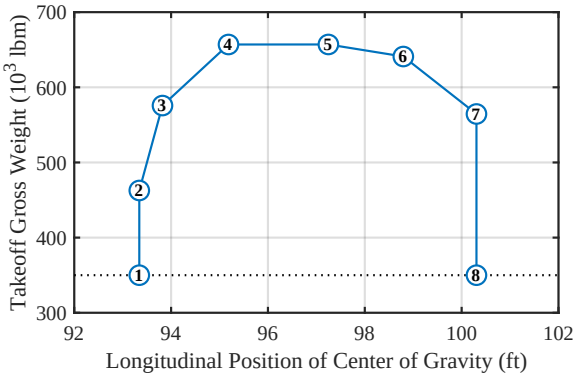

Fig. 11 CG envelope of baseline aircraft

As required by the certification rule, the certification analyses performed by dynamic load and flight characteristics are conducted at multiple flight conditions within the operational limits. The flight envelope of the baseline aircraft is limited by the the maneuver speed V_A, design dive speed V_D, and the service ceiling, as shown in Figure 10. V_D is assumed at 340 knots equivalent airspeed (KEAS), and the service ceiling is assumed at 43 000 ft. V_A is set at 167.7 KEAS, which is derived from the maximum lift coefficient of clean configuration assumed at 1.4 and the limit load factor assumed at 2.5. The operational limits of aircraft weight and center of gravity (CG) location is illustrated in the CG envelope shown in Fig. 11. The CG envelope is derived from the main landing gear loading plot of B777-200ER from the airport planning [32]. Note that for each HT design case, the flight envelope is assumed fixed but the CG envelope is updated with new aircraft mass properties.

2. Subsystem Architecture

The baseline aircraft features a conventional subsystem architecture similar to the B777 aircraft, where all flight control actuation functions are powered by three centralized hydraulic systems pressurized at 3000 psi [34]. Each elevator panel is equipped with two hydraulic actuators. The outboard actuator on the left elevator is powered by #1 hydraulic system, the outboard actuator on the right elevator is powered by #2 hydraulic system, and the inboard actuators on both elevator panels are powered by #3 hydraulic system [35]. The trimmable horizontal stabilizer (THS) is actuated by a single hydraulic actuator powered by two hydraulic systems [35]. Such connectivity ensures that the failure of a single hydraulic system does not affect normal operation of the elevator and THS actuation. The subsystem architecture remains invariant for all design candidates.

B. Design Variables

The design variables for horizontal tail design and optmization include the HT planform geometry variables and elevator geometry variables. The assumptions made with HT geometry and elevator geometry in this paper are as follows:

1) The HT planform is a trapezoid.
2) The location of the trailing edge of HT root is fixed relative to the fuselage.
3) The elevator planform is a trapezoid whose trailing edge is aligned with the HT trailing edge.

With the assumptions above, the geometry of HT is represented by five variables: aspect ratio (ARHT), taper ratio (TRHT), quarter-chord sweep angle (SWPHT), average thickness-to-chord ratio (TCHT), and planform area (SHT). The geometry of elevator is determined by three variables: dimensionless spanwise locations of elevator inboard and outboard extremities (ETAEI and ETAEO) as fractions of HT span, and the ratio of elevator chord length to HT local chord length at the mid-span of elevator (CRE).

The baseline values of these design variables are calibrated from the HT and elevator of the CRM. The design space of interest is constructed by the ranges of design variables as shown in Table 2.

Table 2 Ranges of Design Variables

Design Variable	Minimum	Baseline	Maximum
ARHT	3.70	4.62	5.54
TRHT	0.26	0.33	0.40
TCHT	0.071	0.088	0.106
SWPHT (deg)	27.86	34.82	41.78
SHT (sqft)	895.4	1119	1343
ETAEI	0	0	0.20
ETAEO	0.80	0.93	1.00
CRE	0.233	0.291	0.350

C. Objective Functions

The general aircraft design goal is to maximize performance and minimize cost. The performance includes point performance (e.g. takeoff/landing distance, climb rate, and maneuverability etc.) and mission performance (e.g. range, endurance, and fuel consumption, etc.). In terms of horizontal tail retrofit, both of them are affected by the changes in aircraft drag and operating empty weight due to the new HT. The cost includes manufacturing cost and operational cost. To simplify the cost calculation in early design phase, the manufacture cost can be represented by the aircraft operating empty weight. The operational cost can be represented by the fuel burn at a nominal mission. In this paper, the nominal mission is selected based on the historical operation of the B777-200ER aircraft. Based on the statistics from the U.S. Department of Transportation [36, 37], the mission with a range of 5000 nmi and the same payload as the design payload is selected as the nominal mission.

To summarize, the following three objectives are selected for the HT design and optimization problem:

1) Minimize the overall aircraft drag at design cruise condition (since the reference wing area is invariant, this is equivalent to minimizing the cruise drag coefficient);

2) Minimize the aircraft operating empty weight;
3) Minimize the block fuel for the nominal mission.

D. Constraint Functions

Three types of constraints are considered for the horizontal tail design and optimization: customer design requirements and airworthiness regulations.

Customer design requirement is the design mission range specified in the Request for Proposal. In this paper, since the baseline vehicle is sized based on the mission profile of B777-200ER [32], the design range is selected as 7530 nmi which is the design range of B777-200ER. Therefore, with new-designed HT, the range that can be flown by the aircraft with design mission payload should no less than the required design range. The computation of range is performed by the mission analysis described in Sec. II-G.

Airworthiness regulatory design constraints include the rules from 14 CFR Part-25 Subpart-B Flight and Subpart-C Structure. Subpart-B specifies requirements for aircraft performance and flight characteristics. The rules that are related to HT design in Subpart-B include: §25.107-115 Takeoff, §25.121 Climb: One-engine-inoperative, §25.125 Landing, §25.143 Controllability general, §25.145 Longitudinal control, §25.173-175 Static longitudinal stability, §25.181 Dynamic stability, and their cross-referenced regulations. Subpart-C defines the load conditions that the aircraft structure should be able to sustain. The rules that related to HT structural design in Subpart-C include: §25.331 checked-pitch maneuver, and their cross-referenced regulations. In this paper, the Subpart-B constraints are checked by the Flight Certification Analysis Module as described in Sec. II-H. The Subpart-C constraints are enforced in the HT structural sizing loop and simulated by the Dynamic Load analysis as described, generically, in Sec. II-E. The details of certification constraints analyses are described in following subsections.

1. Subpart-B: Performance and Flight Characteristics Certification Constraints

The Subaprt-B constraint checks include takeoff, climb, landing, stability, and controllability. Among them, takeoff, climb, and landing are checked at maximum weight and reference CG location, while stability and controllability are checked at the eight corner cases in the CG envelope shown in Fig. 11.

Takeoff certification check is to evaluate whether the aircraft with new designed HT and elevator could provide enough control power to maintain the same level of takeoff performance and satisfy the takeoff speed regulatory requirements. For each HT design case, the certification module will iteratively solve the initial elevator deflection for takeoff rotation such that the takeoff field length of the redesigned aircraft could match baseline vehicle value. Once the elevator control is determined, the takeoff trajectory is then computed through the 3-DoF dynamic simulation. The simulation would output the maximum elevator deflection during takeoff to compare with the deflection limit, as well as output the takeoff speeds for constraint check. The takeoff speeds constraints defined in §25.107 are applied on takeoff rotation speed V_R and takeoff safety speed V_2, such that

$$V_R \geq \max(V_1, 1.05V_{mc}) \tag{2}$$

$$V_2 \geq \max(1.13V_{SR}, 1.1V_{mc}) \tag{3}$$

In this paper, the engine failure speed V_{EF}, decision speed V_1, stall speed V_{SR}, and minimum control speed V_{mc} are assumed fixed at baseline vehicle values for all HT design cases.

Climb certification check is to evaluate whether the drag of new HT would compromise the excess power for climb and whether the elevator could provide enough control power to trim the climb. The check is performed by comparing the available steady gradient of climb (i.e. tangent of climb angle) at critical engine inoperative condition against the minimum gradient of climb specified in §25.121. Four flight conditions are involved in climb check as defined by the regulation: 1. Lift-off ($\tan\gamma \geq 0$); 2. Starting point of landing gear retraction, assumed at V_2 ($\tan\gamma \geq 0.024$); 3. Final takeoff point at 1500 feet ($\tan\gamma \geq 0.012$); 4. Approach ($\tan\gamma \geq 0.021$). The available steady available gradient of climb as well as the elevator deflection used to sustain such gradient of climb are computed by longitudinal trim analysis with maximum throttle given to the operating engine.

Landing certification check is to evaluate whether the new HT and elevator could provide enough control power during the flare segment thus to encourage a smooth landing. The check is performed by the landing simulation which starts from the stabilized approach with -3° flight path angle. Once the flare height is reached, the throttle starts to reduce from approach setting to idle, and the elevator control will be determined by the TECS in order to reduce the rate

of descent. According to the Advisory Circular [30], the rate of descent at touchdown constraint is

$$V_\infty \sin\gamma \geq -6 \text{ ft/sec} \tag{4}$$

For all design cases, the gain constants of TECS are assumed fixed to simulate no change in pilot skills. The maximum elevator deflection and the rate of descent at touchdown are output from the landing simulation and compared with the deflection limit and constraint value.

Controllability certification checks includes the coordinated turn check required in §25.143(h) and longitudinal controllability check required by §25.145(b). The coordinated turn check evaluates to whether the aircraft is able to trim with new HT and elevator at asymmetric flight conditions with high angle of attack and bank angle. Due to the coupling between longitudinal and lateral motions at coordinated turn, not only elevator control, but also aileron and rudder controls are examined in this test. The coordinated turn check is performed at four conditions: 1. 30° banked turn with takeoff configuration and critical engine inoperative (CEI) at V_2; 2. 40° banked turn with takeoff configuration and all engine operating (AEO) at $V2$; 3. 40° banked turn with cruise configuration and CEI at V_{FTO}; 4. 40° banked turn with landing configuration and AEO at V_{REF}. On the other hands, the longitudinal controllability check evaluates the controllability to prevent loss of height and velocity during the change of thrust and flap settings. However, due to the lack of unsteady aerodynamic model for flap transition in early design phase, it is difficult to perform the dynamic controllability check. Instead, the certification module performs static trim analysis at four boundary conditions: 1. Extended slats/flaps with idle throttle; 2. Extended slats/flaps with full throttle; 3. Retracted slats/flaps with idle throttle; 4. Retracted slats/flaps with full throttle. The differences in elevator deflections at these four conditions are computed to check whether the aircraft can be trimmed at the other conditions if previously trimmed at one condition. The maximum difference is output from the analysis and compared with both the elevator upward and downward deflection limits.

Stability certification check evaluates the aircraft longitudinal static and dynamic stability with new HT as required by §25.173, §25.175, and §25.181. The check is performed by an eigenmode analysis using the certification module. Assume small disturbance, the system dynamic equation can be written as

$$\dot{\mathbf{X}} = A\mathbf{X} + B\mathbf{U} \tag{5}$$

where $\mathbf{X}$, $\mathbf{U}$ are the state and control vectors, and A, B the derivative matrices. In the stability check, the eigen-mode analysis is applied on A matrix. The derivatives of the A matrix are computed numerically in the certification module. The longitudinal eigenvalues of A matrix are expected to be two complex conjugate pairs. Although the certification rule does not specify any quantitative constraints for stability, the certification module applies the criteria from the military specification MIL-F-8785C [38] to further evaluate the aircraft handling quality, as shown in Tables 3 and 4. Suppose the conjugate complex eigenvalue is

$$\lambda = -\sigma \pm j\omega_d \tag{6}$$

The damping ratio ξ_d and the time to double amplitude T_2 are computed as

$$\xi_d = \frac{\sigma}{\sqrt{\sigma^2 + (\omega_d)^2}} \tag{7}$$

$$T_2 = \frac{\ln 2}{|\sigma|} \tag{8}$$

Table 3 Phugoid handling quality [38]

Level	**Minimum ξ_d**	**Minimum T_2**
1	0.04	-
2	0	-
3	-	55 seconds

Table 4 Short-period damping ratio limits [38]

Level	Takeoff & Landing		Cruise	
	Minimum	Maximum	Minimum	Maximum
1	0.35	1.30	0.30	2.00
2	0.25	2.00	0.20	2.00
3	0.15	-	0.15	-

2. Subpart-C: Checked Pitch Maneuver Certification Constraint

The checked pitch maneuver (nose up or nose down) consists of a pitching motion of the aircraft generated through control input from the pilot which is then checked, or stopped with opposite control input. The maneuver is precisely described in the text of §25.331(c)(2) in terms of control deflection as a function of time, achieved load factor, and pilot force. The function that describes the yoke displacement over time is given as

$$\delta(t) = \delta_{max} \sin(\omega t), \quad \text{for} \quad 0 \leq t \leq t_{max} \quad \text{and} \quad \omega \leq \omega_{max} \tag{9}$$

with:

- δ_{max}: the maximum yoke deflection, as limited by the control system stops, control surface stops, or by pilot effort as prescribed in §25.397.
- $t_{max} = \frac{3\pi}{2\omega}$
- ω: circular frequency (rad/sec) of the control deflection taken equal to the undamped natural frequency of the short period rigid mode of the aircraft, with active control system effects included where appropriate.
- $\omega_{max} = \frac{\pi V}{2V_A}$: with V the speed of the airplane at entry of the maneuver and V_A the design maneuvering speed.

Equation 9 is modified to account for achievable load factors. If the maximum load factor is not reached with the control input specified by Eq. 9, then the pilot must hold the control surface deflected until the load factor is reached but for no more than five seconds. On the other hand, the maximum prescribed positive load factor must not be exceeded. In such cases, the flight deck pitch control deflection amplitude should be scaled down. Figure 12 shows examples of these types of longitudinal control inputs.

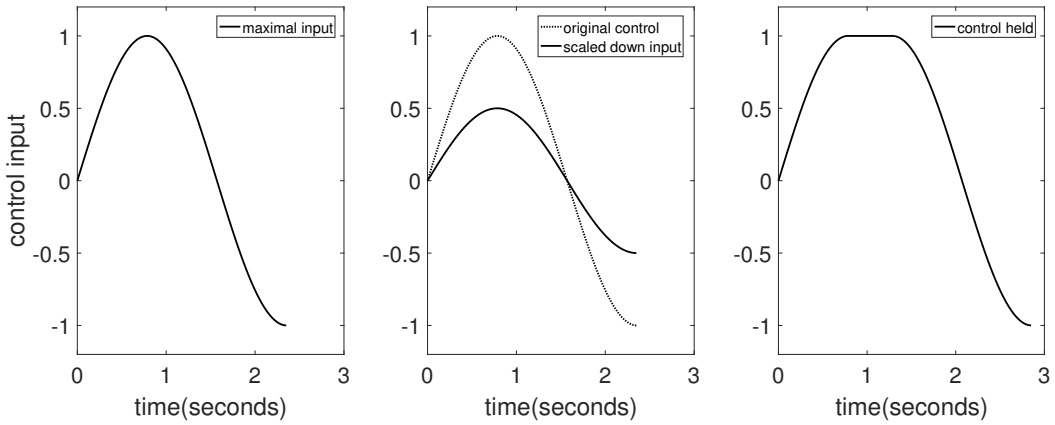

Fig. 12 Examples of control inputs. Left: Prescribed sinusoidal control input; Center: Control input scaled down to avoid exceeding limit load factor; Right: Full control input held to allow load factor to build

Furthermore, the loads do not need to be recorded after the time for which the load factor goes below zero (respectively above 2.5) during the second phase of the nose up (respectively nose down) maneuver, in which case the simulation can be stopped. Also, the simulation may be stopped if the effort required by the pilot to control the airplane falls outside the ranges prescribed by §25.397. For this work, the upper bound of 300 lbf is employed.

Simulations must be performed for maneuver entry speeds between the design maneuvering speed V_A and the design dive speed V_D. In order to correctly implement §25.331(c)(2), the checked pitch maneuver must then be performed for

several points in the aircraft flight envelope corresponding to speeds between those two values. The flight condition is defined by the entry speed, starting altitude, and loadout of the aircraft (weight and CG position). For each flight condition, the dynamics of the aircraft are different. Consequently, both the circular frequency of the control input ω and the maximum control deflection δ_{max} need to be computed for each case in order to generate the appropriate control input for the pilot. The flight conditions and CG envelope used in the testing are described in Section. 1.

Figure 13 shows a flowchart that summarizes the overall process for the certification-driven flight simulation for a single case from the testing envelope. It is created using an Extended Design Structure Matrix (xDSM). Starting with an altitude, Mach number and weight configuration, the trim algorithm is run to determine the trim controls to put the airplane in steady, level flight. At this point, the Equations of Motion (EoM) are linearlized about the trim point to obtain A and B matrices. The A matrix allows for the determination of the short period characteristics. Once the circular frequency of the FAR control input has been set, an iterative process is necessary to comply with the certification requirements on the maximum (for nose up maneuver) or minimum (for nose down maneuver) achieved load factor. This is represented by the $2, 5 \rightarrow 3$ loop in the flowchart. The goal of this iterative process is to determine the flight deck pitch control input for the pilot which complies with §25.331(c)(2) as described in Eq. (9) and Figure 12. Finally, once the correct pitch control input has been established, a final checked pitch maneuver is run, and all the quantities of interest are recorded during the course of the maneuver.

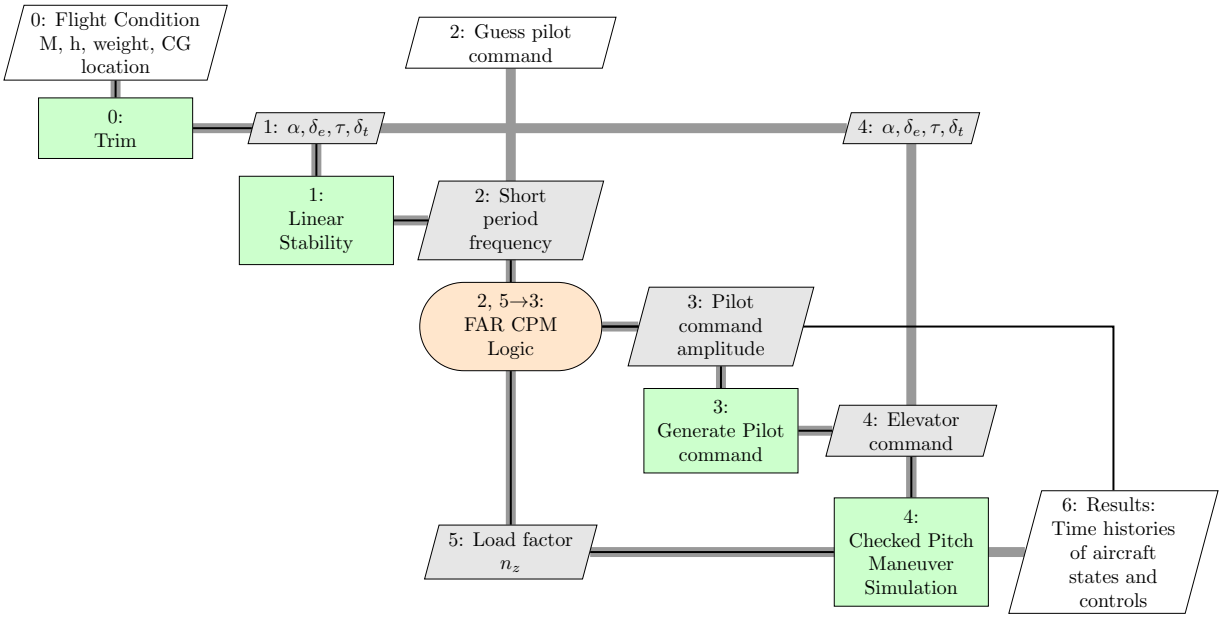

Fig. 13 Maneuver simulation flowchart

IV. Results

A. Design Space Exploration

The framework described in Section II is computationally faster due to the use of lower-fidelity analysis tools. However, for effective design space exploration, it is still too slow. For computationally expensive simulations, surrogates can be used to approximate the input-output relationship.

1. Surrogate Modeling

To effectively sample the design space in the design variable ranges shown in Table 2, a Design of Experiments (DoE) was conducted. 193 samples were generated using a combination of face-centered central composite and Box-Behnken methods, and 600 using Latin hypercube method. Another 200 samples were randomly generated to serve as validation cases. The 993 cases were run through the framework to obtain responses of interest. The responses were fit against the

design variables using either a neural network or a multivariate polynomial regression using statistical software JMP.

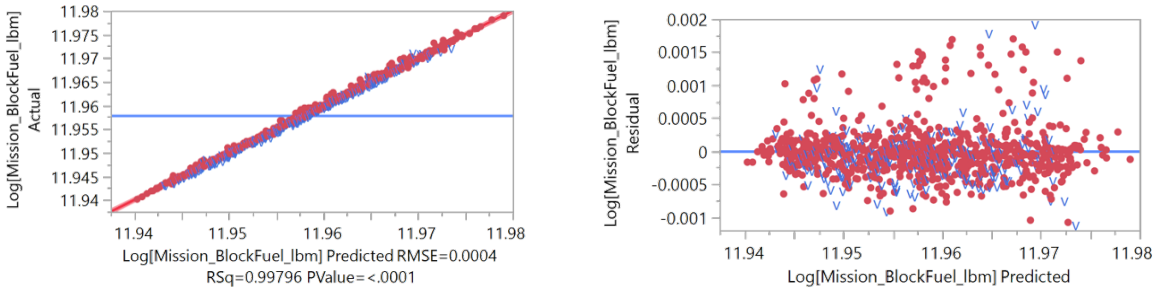

(a) Actual vs. predicted plot **(b) Residual vs. predicted plot**

Fig. 14 Goodness of fit plots for block fuel consumption response

All models were checked to see if they are good enough to serve as surrogate models. The tables in Appendix B give the values of R^2 and square root of the mean squared prediction error (RMSE) for all the responses. The actual vs predicted plots and residual vs predicted plots were checked to ensure the surrogate model is valid. An actual vs predicted plot (for example, Fig. 14a) shows the actual values of the response plotted against the predicted equation for the response based on the assumed functional form. A good surrogate will show data points randomly scattered about zero residual in the residual vs predicted plot (for example, Fig. 14b). For the response shown, the fit is reasonably good. An in-depth explanation of generating and validating surrogate models using DoEs is given in Mavris et al. [39].

2. Feasibility Test

The surrogate model may now be employed to perform probabilistic design. First, an estimate of the percentage of feasible alternatives in design space is necessary. This analysis was meant to provide insight regarding which constraints are active or inactive, and if any, "show-stopper" constraints which lead to failure of the entire design space, and the relative importance of the design variables. A random uniform sampling of 1 000 000 cases within the design space (Table 2) was evaluated using the surrogate models. A Cumulative Distribution Function (CDF) was plotted for each constraint to determine the feasibility of the design space. All CDF plots are shown in Appendix C.

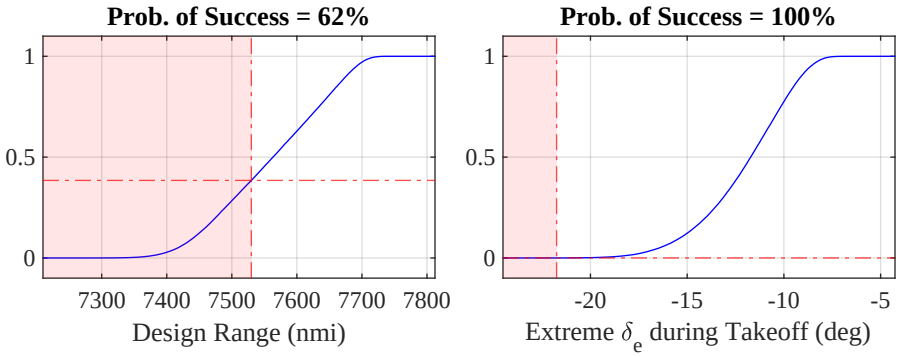

Fig. 15 Examples of cumulative distribution function for constraints

Two example CDF plots are presented in Fig. 15 illustrating the activity of given constraints: the critical value of a constraint is marked as a vertical dashed line, dividing the plot into shaded infeasible region and un-shaded feasible region; the rise of CDF curve in the feasible region is regarded as the *probability of success*, i.e. the fraction of design space which satisfies the particular constraint. A probability of success of 100% indicates that the constraint is inactive and has no impact on the feasible design space; a probability of success between 0 and 100% indicates that the constraint may actively constrain the feasible design space; a probability of success of 0 indicates that the constraint is a "show-stopper", and action must be taken, such as relaxing the constraint and/or expanding the design space, to obtain a nonempty feasible design space.

In the examples in Fig. 15, first consider the design range constraint. The aircraft is required to travel at least 7530 nmi for the design mission. The CDF plot shows that 62% of the cases in the Monte Carlo simulation satisfy this constraint. Next consider the CDF for extreme elevator deflection δ_e during take-off. The elevator travel limit is $-30°$ upward and $25°$ downward. To account for the aleatory uncertainties in flight tests as well as the epistemic uncertainties in analysis models, the constraint selected for elevator in this section is confined to 70% of the travel limit, thus $-21.8°$ as the upward deflection limit as seen in the plot. The CDF plot shows that every design in the Monte Carlo simulation satisfies the elevator deflection constraint. Therefore, the design range constraint is active and will be carried through subsequent analyses, whereas the constraint of extreme elevator deflection δ_e during take-off is inactive.

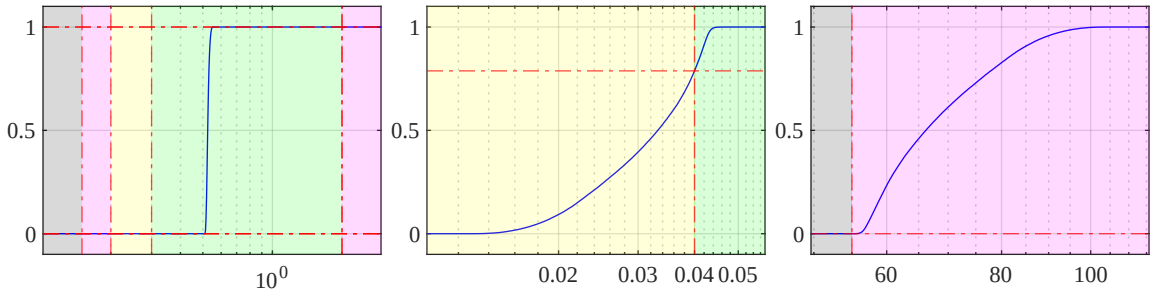

(a) Cruise Config. Short Period Mode ξ_d **(b) Takeoff Config. Phugoid Mode ξ_d** **(c) Landing Config. Phugoid Mode T_2 (sec)**

Fig. 16 Handling qualities Cumulative Distribution Function for CG case 2

The CDFs of handling quality constraints are presented in Fig. 25 and 26 in Appendix C whose threshold values are based on MIL-F-8785C [38]. The stability check was performed at the eight corner cases of the CG envelope (Fig. 11). To demonstrate the capability of relaxing constraints, case 2 and case 5 are selected for feasibility analysis, since the DoE statistics show that handling qualities of both level 1 and level 2 exist among the sample cases.

Figure 16 presents examples of CDF plots for handling quality extracted from Fig. 25. Each plot is divided into regions based on the threshold values in Table 3 or 4, explained below:

1) Short period mode
   - The green region in the ξ_d plot covers handling quality of Level 1 (*desirable*)
   - The yellow region in the ξ_d plot covers handling quality of Level 2 (*acceptable*)
   - The magenta region in the ξ_d plot covers handling quality of Level 3 (*poor*)
   - The gray region in the ξ_d plot falls outside handling quality categorization (*infeasible*)
2) Phugoid mode
   - The green region in the ξ_d plot covers handling quality of Level 1 (*desirable*)
   - The yellow region in the ξ_d plot covers handling quality of Level 2 (*acceptable*) or worse
   - The magenta region in the T_2 plot covers handling quality of Level 3 (*poor*) or better
   - The gray region in the T_2 plot falls outside handling quality categorization (*infeasible*)

For each CDF plot for handling quality metrics, the rise of CDF curve within each region represents the fraction of simulated cases which fall within the respective region. According to Fig. 25 and 26, the entire design space satisfies the short period mode level 1 handling qualities for all configurations and both CG envelope cases, since the CDF curve rises from 0 to 1 in the green region in all CDF plots for short period mode ξ_d. The phugoid mode handling quality is evaluated using the CDF plots of both ξ_d and T_2. Based on the CDF plots for phugoid mode T_2 in Fig. 25 and 26, the entire design space is deemed at level 3 (feasible but poor) or better for all configurations and both CG envelope cases. For cruise and landing configurations, based on the CDF plots for phugoid mode ξ_d in Fig. 25 and 26, the entire design space satisfies the level 1 (desirable) handling quality criteria for both CG envelope cases. The cross-hair in Fig. 16 (b) indicates that, for takeoff configuration at CG envelope case 2, 21% of the simulated cases satisfy the level 1 criteria (desirable); however, if the handling quality requirement for takeoff phugoid mode is relaxed from level 1 to level 2, then all cases would satisfy the requirement. Similar observation and action can also be taken for takeoff configuration at CG envelope case 5 based on Fig. 26.

The discussion above illustrates how Monte Carlo simulations (performed using a surrogate model) can be used to determine active and inactive constraints and the feasible region in the design space. For the test case in this work, the

list of active constraints are: design range, rate of descent at touchdown, phugoid mode at take-off configuration, and coordinated turn rudder trim at take-off configuration critical engine inoperative. Note that the design variables pertain to the horizontal tail, but the framework evaluates constraints pertaining to the entire aircraft. It is seen that the rudder, which is not influenced by the design variables, is an active constraint in the optimization.

B. Multi-objective Optimization

Figure 17 shows a scatter-plot matrix for the objectives, in which the solution space is projected onto three bi-variate planes. Each point in the scatter-plot represents an individual case from the Monte Carlo simulation. The active constraints, except for handling quality, are applied to filter out the infeasible designs. The handling quality constraint is sequentially activated following the evaluation criteria at different levels, as indicated by different colored regions. The preferred designs where the handling quality metrics fall in level 1 are highlighted in blue, which only occupy a small portion of design space. The designs in red and black are the feasible with acceptable handling quality, i.e. at least one handling quality metric falls in level 2. Note that the authors did not perform a gradient-based or global optimization, therefore the *optimum* refers to the best case found from the Monte Carlo simulation runs.

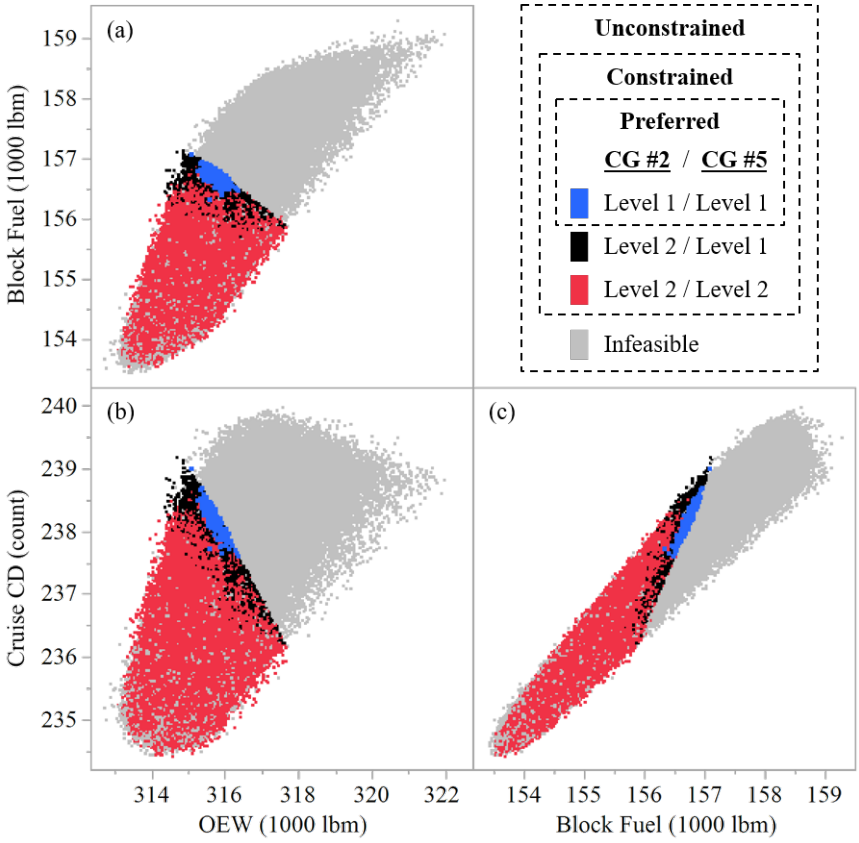

Fig. 17 Scatter-plot matrix of filtered Monte Carlo simulation

Because the three objectives–cruise drag, operating empty weight, and block fuel–are all to be minimized, the non-dominated cases towards the bottom left corner in each scatter-plot form the Pareto frontier for the respective pair of objectives. It is seen from Fig. 17 that the Pareto frontier is pushed back as the constraints become active. Figure 18 shows the unconstrained single-objective optimal designs. Comparing these three unconstrained optimal designs, the optimal design for operating empty weight has the lowest sweep angle and aspect ratio and highest thickness-to-chord ratio, while the optimal design for cruise drag is similar to the optimal design for fuel burn.

When the constraints are activated and different levels of handling quality requirements are applied, the Pareto optimal designs change subsequently. The nine optimal designs for the three objectives and three scenarios (unconstrained, constrained, and preferred) are cross-compared in Fig. 19 and 20, where the aerodynamic centers of all designs are

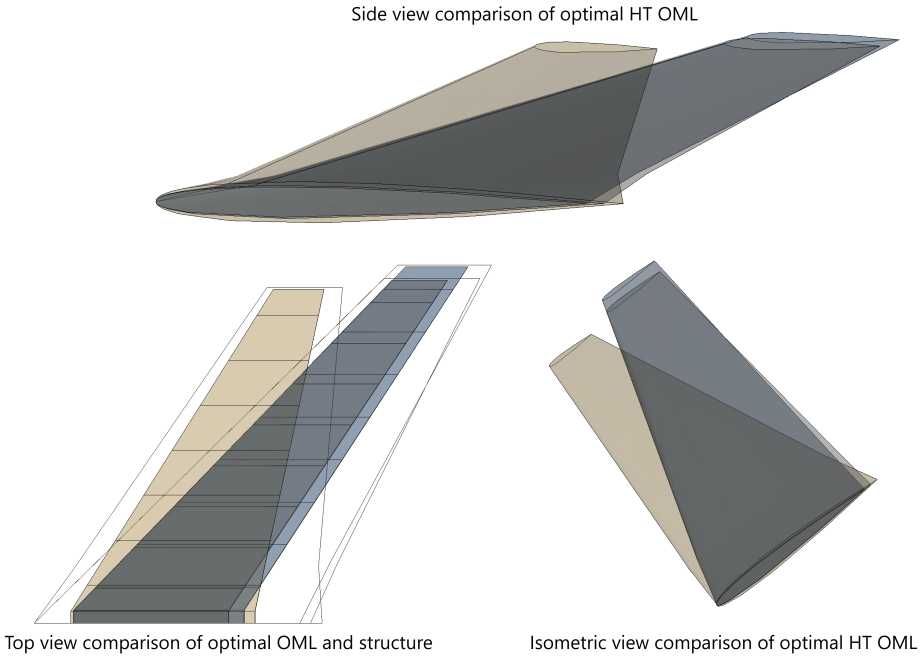

Fig. 18 Unconstrained optimal designs considering only C_D objective (blue), OEW objective (gold), and Fuel Burn objective (gray)

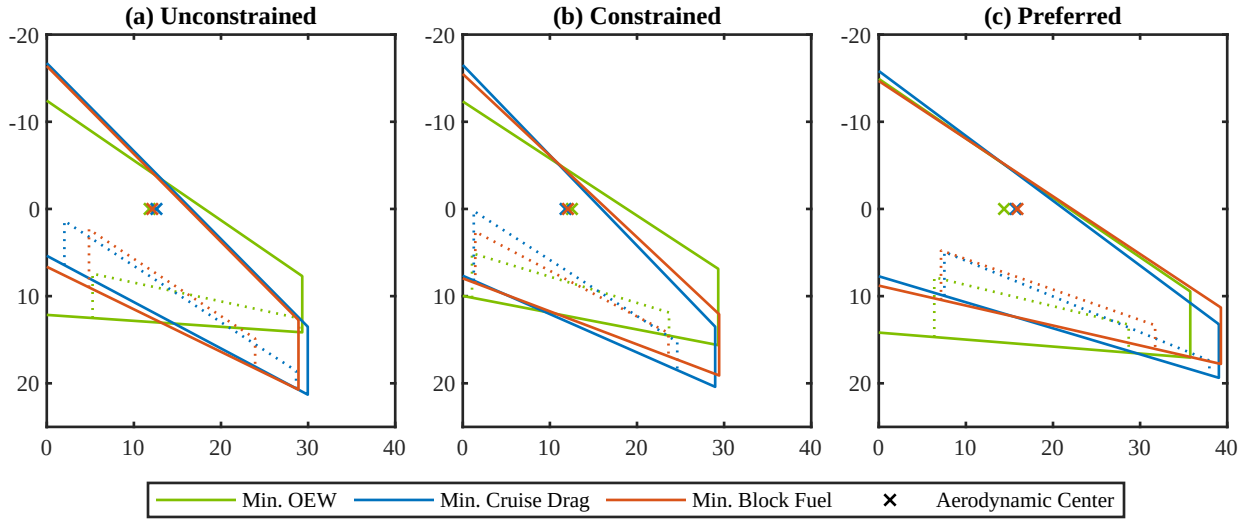

Fig. 19 Optimum horizontal tail planform design for the three objective functions (dimensions in ft)

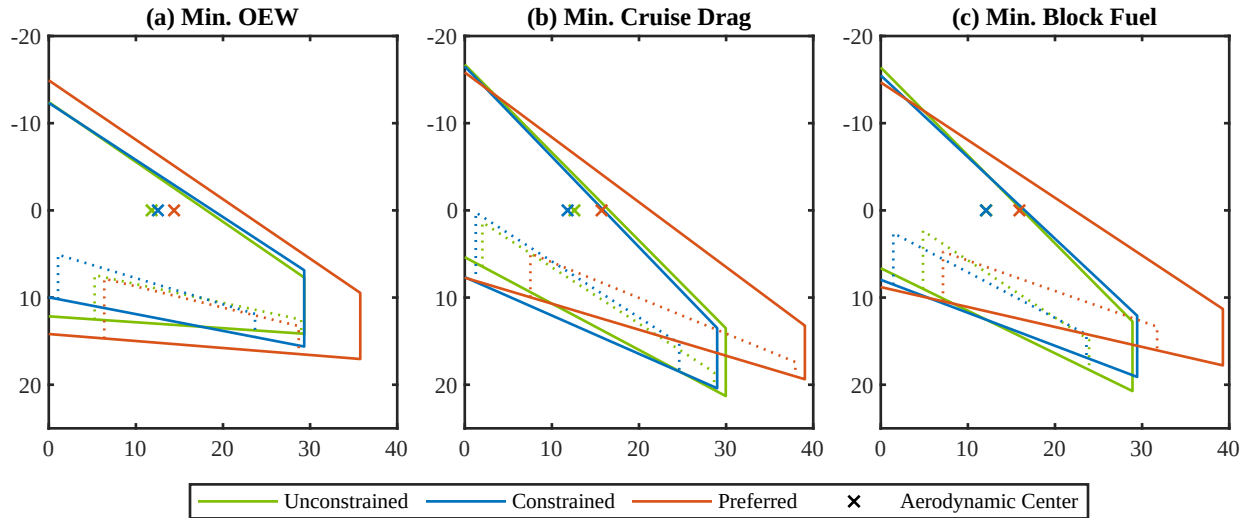

Fig. 20 Horizontal tail planform design highlighting the difference between unconstrained, constrained and preferred optima (dimensions in ft)

aligned at the same longitudinal position. Each subplot in Fig. 19 compares the single-objective optima for a given scenario. It is seen from the comparison that the elevator size of the optimal designs with constraints are larger than unconstrained cases, and the HT size is significantly increased if level-1 handling quality is required. Another comparison is performed between unconstrained, constrained, and preferred optima for a given objective, as shown in Fig. 20. The comparison shows that lower sweep angle and aspect ratio are favored to minimize OEW, but are disadvantageous in drag and block fuel reduction. The similar planform geometry between drag minimization and block fuel minimization cases also reveals that the HT drag is more correlated to fuel burn than the operating empty weight.

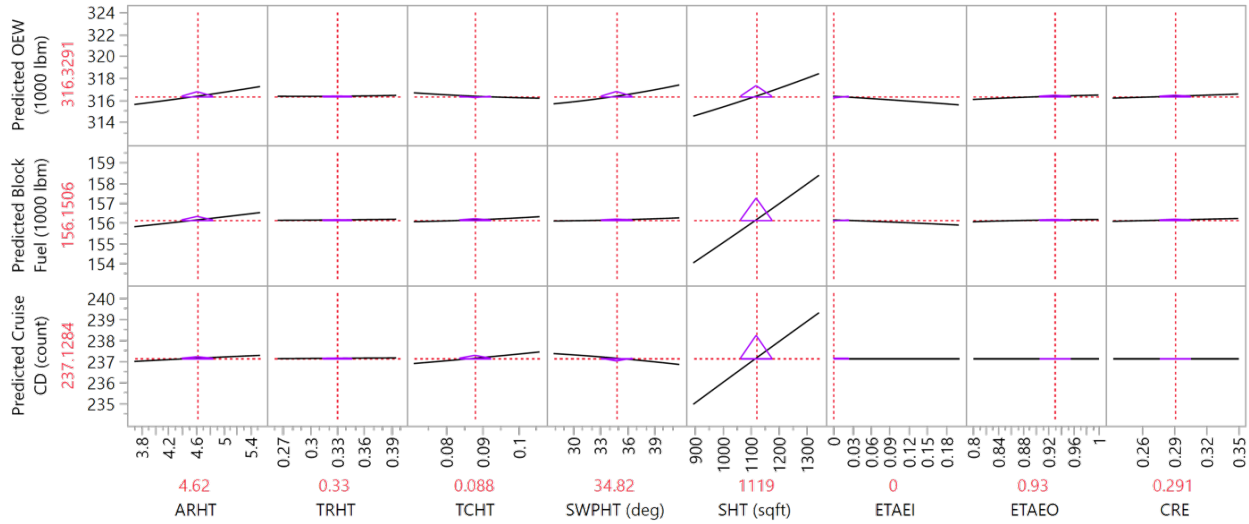

Fig. 21 Snapshot of profiler plots for design objectives vs. design variables at baseline settings

It should be noted that the surrogate model also allows for the creation of a prediction profiler as shown in Fig. 21. The profiler illustrates the sensitivities of the objective functions to the design variables as indicated by the local slope of each response curve at the crosshair and the direction and height of the triangular indicators. It is seen that the horizontal tail planform area (SHT) has the largest impact, whereas the elevator variables–ETAIE, ETAOE, and CRE–do not greatly impact the objective functions. The drastic differences in elevator planform design seen in Fig. 20(b) are an artifact of the Monte Carlo simulation.

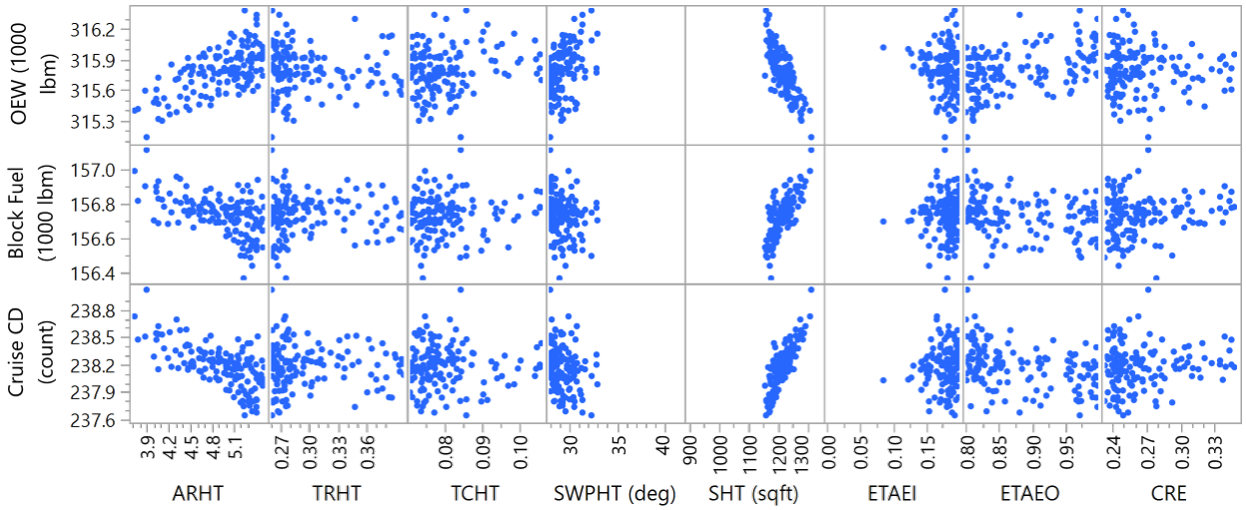

Fig. 22 Scatter-plot matrix for preferred designs

V. Future Work

Avenues for future work utilizing and extending the capabilities of the developed framework include are discussed next. The dynamic loads generation in this work were performed assuming rigid-body flight dynamics. The regulations state that the flexibility of the structure must be accounted for while performing the maneuvers. One such study was performed in a prior work by Sarojini et al. [27], where the structure was represented as beams and coupled with the aerodynamics and flight dynamics. The DELPHI framework described in Section II-E will be extended to allow for flexible flight dynamics.

The aerodynamic characteristics obtained by AVL (Section B and mass properties of subsystems (Section D), while better than using purely empirical data, are still subject to epistemic uncertainty due to their low fidelity. The uncertainty will translate to variability in the predicted structural loads during dynamic maneuvers, and hence affect structural sizing, and by extension, the final mission level properties.It is desirable for the designer/analyst to know (i) the extent to which the different critical loads are impacted by uncertainty and (ii) the relative influence of the identified sources of uncertainty on the observed variability of the maneuver loads.

The subsystems were simplified in this work by neglecting detailed time-consuming analysis of irrelevant subsystems such as the environmental control system. Considering additional subsystems such as thermal ice protection systems [40] and electrical subsystems [41] would give a better estimate of the OEW. The computationally slowest part of the framework is the structural analysis. Further, the dynamic loads were converted into equivalent static loads. Simplifying the structure to beams [42, 43] and sizing directly for dynamic loads using adjoint-based gradient optimization [44] would ease the computational burden.

Appendix

A. Geometry and Performance Specifications of the Baseline Aircraft

Table 5 Specifications of baseline aircraft

Parameter	Value	Unit
Passenger capacity	305	-
Design range	7530	nmi
Cruise Mach number	0.84	-
Sea-level static thrust	$2 \times 97\,300$	lb
Maximum ramp weight	657 000	lb
Maximum landing weight	460 000	lb
Reference longitudinal center of gravity	97.25	ft
Wing planform area	4927.3	ft^2
Wing aspect ratio	8.81	-
Wing taper ratio	0.18	-
Wing 1/4-chord sweep	30.94	deg
Wing dihedral	7.41	deg
Aileron chord ratio	0.17	-
Aileron extremities (fraction of semi-span)	0.78; 0.98	-
Aileron deflection limits	$-30/+30$	deg
Fuselage total length	206.50	ft
Maximum fuselage width	20.76	ft
Maximum fuselage height	20.23	ft
Horizontal tail planform area	1119.2	ft^2
Horizontal tail aspect ratio	4.62	-
Horizontal tail taper ratio	0.33	-
Horizontal tail 1/4-chord sweep	34.82	deg
Elevator chord ratio	0.29	-
Elevator extremities (fraction of semi-span)	0.07; 0.94	-
Elevator deflection limits	$-30/+25$	deg
Vertical tail planform area	527.84	ft^2
Vertical tail aspect ratio	1.84	-
Vertical tail taper ratio	0.30	-
Vertical tail 1/4-chord sweep	40.03	deg
Rudder chord ratio	0.31	-
Rudder extremities (fraction of semi-span)	0; 0.93	-
Rudder deflection limits	$-27.3/+27.3$	deg

B. Surrogate Model Goodness of Fit Metrics

This section documents the goodness of fit metrics for the design objectives and constraints relevant to the use case in this work.

- In Table 6, "LR" stands for multivariate linear regression, and "NN" for neural network. "log" implies that a logarithm transformation was performed on the respective response to obtain a better surrogate model than using the original data; where applicable, the model error and RMSE were calculated based on the transformed response values.
- In Table 7, the responses were not transformed when creating the surrogate models; the model error and RMSE were calculated based on the original response values.
- In Table 8 and 9, multivariate linear regression was used to create surrogate models for all responses. A logarithm transformation was performed on all responses, and the model error and RMSE were calculated based on the transformed response values.

Table 6 Surrogate model goodness of fit metrics for design objectives, performance requirement, certification requirements §25.107, §25.111, §25.121, §25.125, and §25.145

				R-squared		RMSE	
Category	**Item**	**Unit**	**Model**	**Training**	**Validation**	**Training**	**Validation**
Design objective	OEW	lbm	LR (log)	0.9839	0.9774	5.96E-04	5.99E-04
Design objective	Block fuel	lbm	LR (log)	0.9980	0.9971	3.88E-04	4.02E-04
Design objective	Cruise C_D	–	LR (log)	0.9999	0.9999	5.94E-06	6.67E-06
Performance req.	Design range	nmi	LR (log)	0.9943	0.9916	9.39E-04	9.88E-04
§25.107(c)	V_2/V_{SR}	–	NN (log)	0.8540	0.7059	3.48E-04	4.37E-04
§25.107(c)	V_2/V_{MC}	–	NN (log)	0.8541	0.7067	3.48E-04	4.36E-04
§25.107(e)	V_R/V_{MC}	–	LR (log)	0.9963	0.9914	5.07E-04	6.66E-04
§25.111	δ_e	deg	LR	0.9986	0.9961	9.57E-02	1.38E-01
§25.121(a)	Climb gradient	–	LR	0.9838	0.9584	2.05E-05	2.81E-05
§25.121(b)	Climb gradient	–	LR	0.9978	0.9960	1.53E-05	1.91E-05
§25.121(b)	δ_e	deg	LR	0.9974	0.9943	5.29E-02	6.87E-02
§25.121(c)	Climb gradient	–	NN	0.9211	0.8299	2.49E-05	3.15E-05
§25.121(c)	δ_e	deg	LR	0.9983	0.9963	3.50E-02	4.30E-02
§25.121(d)	Climb gradient	–	NN	0.9844	0.9738	6.62E-05	8.53E-05
§25.121(d)	δ_e	deg	LR	0.9950	0.9904	9.84E-02	1.20E-01
§25.125	Rate of descent	ft/sec	LR	0.9821	0.9472	2.18E-01	3.36E-01
§25.125	δ_e	deg	LR	0.9962	0.9930	4.52E-02	5.59E-02
§25.145(b)	δ_e	deg	LR	0.9984	0.9959	7.95E-02	1.10E-01

Table 7 Surrogate model goodness of fit metrics for §25.143(h)

				R-squared		RMSE	
Configuration	**Item**	**Unit**	**Model**	**Training**	**Validation**	**Training**	**Validation**
Takeoff, CEI	δ_e	deg	Linear regression	0.9981	0.9953	2.26E-02	3.00E-02
Takeoff, CEI	δ_r	deg	Neural network	0.9968	0.9766	5.59E-02	1.73E-01
Takeoff, CEI	δ_a	deg	Neural network	0.9942	0.9833	3.54E-02	5.94E-02
Takeoff, AEO	δ_e	deg	Linear regression	0.9985	0.9963	3.30E-02	4.32E-02
Takeoff, AEO	δ_r	deg	Neural network	0.9891	0.9682	1.56E-02	3.12E-02
Takeoff, AEO	δ_a	deg	Neural network	0.9476	0.9302	3.99E-02	4.40E-02
Cruise, CEI	δ_e	deg	Linear regression	0.9981	0.9955	3.98E-02	5.24E-02
Cruise, CEI	δ_r	deg	Neural network	0.9968	0.9772	5.18E-02	1.55E-01
Cruise, CEI	δ_a	deg	Neural network	0.9940	0.9781	2.09E-02	4.12E-02
Landing, AEO	δ_e	deg	Linear regression	0.9961	0.9919	8.99E-02	1.12E-01
Landing, AEO	δ_r	deg	Neural network	0.9953	0.9639	9.97E-03	3.05E-02
Landing, AEO	δ_a	deg	Neural network	0.9928	0.9826	2.02E-02	3.34E-02

Table 8 Surrogate model goodness of fit metrics for §25.181(h) for CG envelope case 2

		R-squared		RMSE	
Configuration	**Item**	**Training**	**Validation**	**Training**	**Validation**
Cruise	Short period mode ξ_d	0.9986	0.9977	4.94E-04	6.59E-04
Cruise	Phugoid mode ξ_d	0.9992	0.9980	9.37E-04	1.35E-03
Cruise	Phugoid mode T_2	0.9788	0.9653	9.09E-04	1.13E-03
Takeoff	Short period mode ξ_d	0.9994	0.9989	2.88E-04	4.02E-04
Takeoff	Phugoid mode ξ_d	0.9963	0.9917	1.67E-02	2.29E-02
Takeoff	Phugoid mode T_2	0.9955	0.9900	1.65E-02	2.28E-02
Landing	Short period mode ξ_d	0.9996	0.9993	3.04E-04	3.92E-04
Landing	Phugoid mode ξ_d	0.9990	0.9978	5.30E-03	7.32E-03
Landing	Phugoid mode T_2	0.9986	0.9969	5.20E-03	7.20E-03

Table 9 Surrogate model goodness of fit metrics for §25.181(h) for CG envelope case 5

		R-squared		RMSE	
Configuration	**Item**	**Training**	**Validation**	**Training**	**Validation**
Cruise	Short period mode ξ_d	0.9988	0.9980	5.23E-04	7.06E-04
Cruise	Phugoid mode ξ_d	0.9991	0.9986	5.36E-04	6.37E-04
Cruise	Phugoid mode T_2	0.9978	0.9969	1.32E-03	1.52E-03
Takeoff	Short period mode ξ_d	0.9993	0.9988	3.18E-04	4.27E-04
Takeoff	Phugoid mode ξ_d	0.9999	0.9997	6.15E-04	7.90E-04
Takeoff	Phugoid mode T_2	0.9998	0.9997	9.06E-04	1.05E-03
Landing	Short period mode ξ_d	0.9995	0.9990	2.26E-04	3.21E-04
Landing	Phugoid mode ξ_d	0.9939	0.9921	1.48E-03	1.76E-03
Landing	Phugoid mode T_2	0.9997	0.9992	3.79E-04	5.33E-04

C. Cumulative Distribution of Constraint Variables

Cumulative Distribution Functions (CDF) for design range and certification constraints are plotted. Fig. 23 shows the certification constraints for §25.143(h) constant speed coordinated turn maneuvering capabilities. Fig. 24 shows the constraints for design range and certification constraints §25.107 takeoff speed, §25.121 one-engine-inoperative climb, §25.125 landing, and §25.145(b) longitudinal controllability. Fig. 25 and Fig. 26 show the longitudinal stability and handling quality constraints §25.173, §25.175, and §25.181 for CG envelope corner case 2 and case 5 respectively.

Table 10 gives the travel limit, and constraints imposed for the control surfaces. To account for the aleatory uncertainties in flight tests as well as the epistemic uncertainties in analysis models, the constraint selected for control surfaces may be confined to values lower than their travel limit. Note that such confinement is not applied to aileron because the spoiler is not included in rolling control, which gives the margin for the uncertainties in lateral maneuvers.

Table 10 Control surface limits

Control Surface	Travel Limit		Constraint	
	Lower	Upper	Lower	Upper
Elevator	-30	25	-21.8	16.8
Aileron	-30	30	-30	30
Rudder	-27.3	27.3	-23.2	23.2

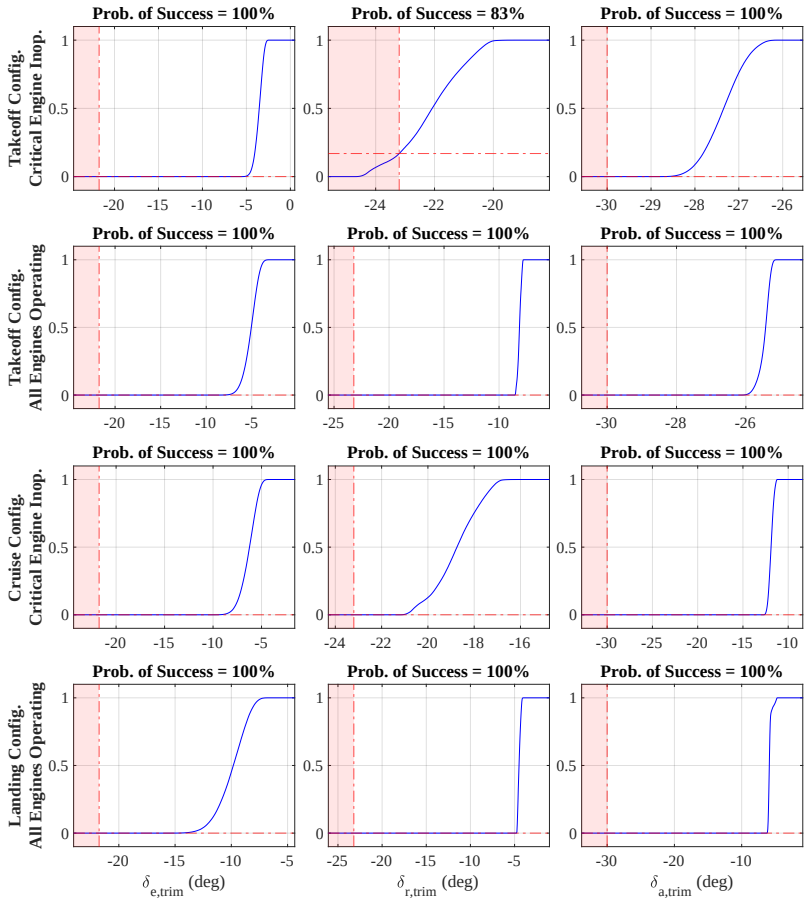

Fig. 23 CDFs of certification requirement §25.143(h)

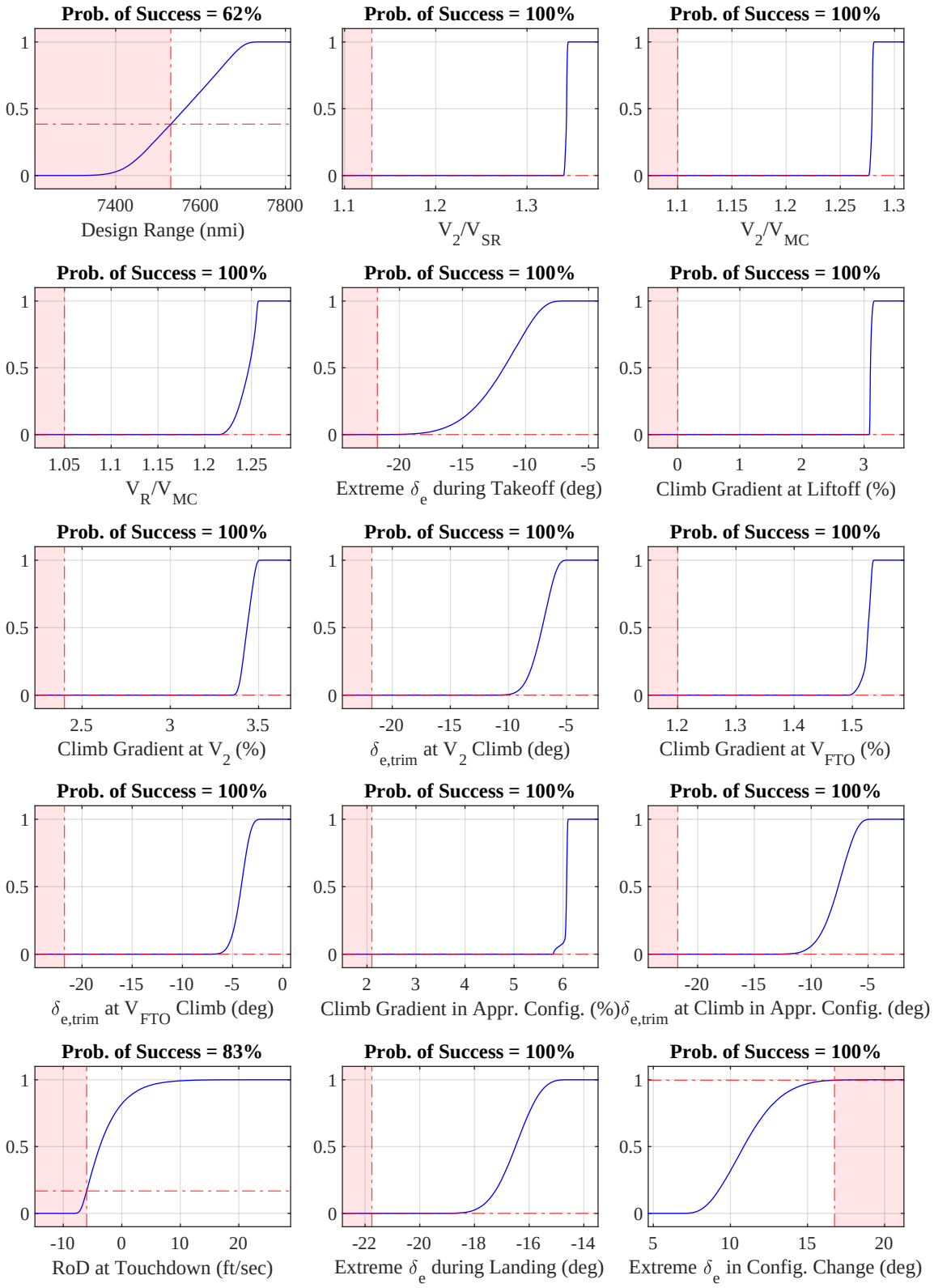

Fig. 24 CDFs of design range constraint, certification requirements §25.107, §25.121, §25.125, and §25.145.

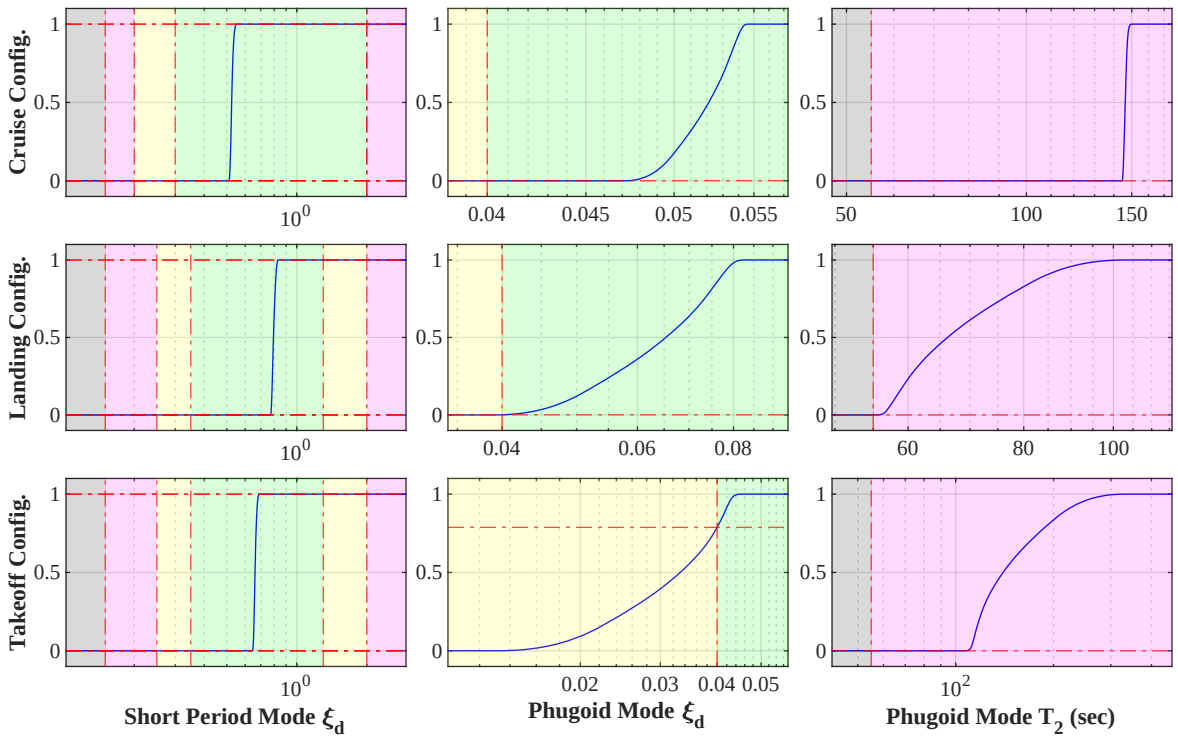

Fig. 25 CDFs of certification requirement §25.173, §25.175, and §25.181 at CG envelope case 2

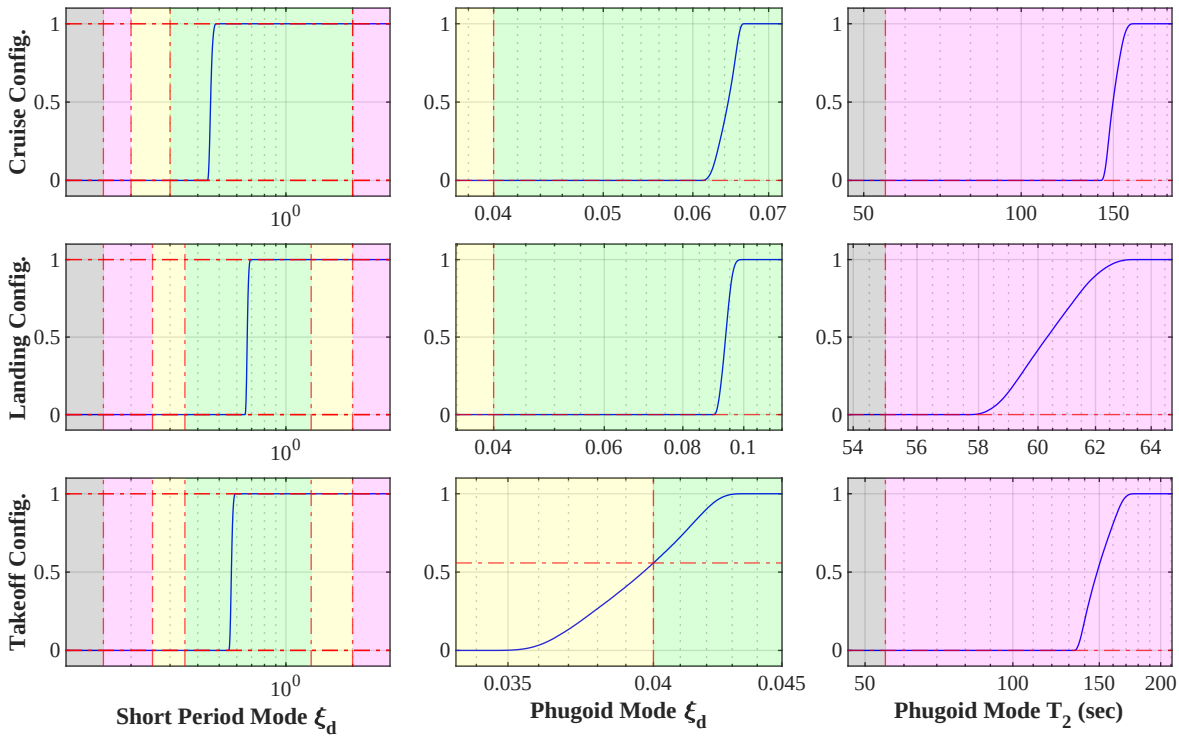

Fig. 26 CDFs of certification requirement §25.173, §25.175, and §25.181 at CG envelope case 5

Acknowledgments

The authors would like to acknowledge Dr. Evan Harrison for helping in the development of the dynamic simulation environment, Mr. Yicong Fu for providing additional computational resources to execute the DoE cases, and Dr. Burak Bagdatli for helping in formulating the test case.

References

[1] McCullers, L., "Aircraft configuration optimization including optimized flight profiles," *Proceedings of a Symposium on Recent Experiences in Multidisciplinary Analysis and Optimization*, 1984, pp. 395–412.

[2] Kirby, M., and Mavris, D., "The environmental design space," *26th international congress of the aeronautical sciences*, Vol. 26, Citeseer, 2008, pp. 2008–4.

[3] Lukaczyk, T. W., Wendorff, A. D., Colonno, M., Economon, T. D., Alonso, J. J., Orra, T. H., and Ilario, C., "SUAVE: An Open-Source Environment for Multi-Fidelity Conceptual Vehicle Design," *16th AIAA/ISSMO Multidisciplinary Analysis and Optimization Conference*, American Institute of Aeronautics and Astronautics, 2015. doi:10.2514/6.2015-3087.

[4] Druot, T., Belleville, M., Roches, P., Gallard, F., Peteilh, N., and Gazaix, A., "A Multidisciplinary Airplane Research Integrated Library With Applications To Partial Turboelectric Propulsion," *AIAA Aviation 2019 Forum*, 2019. doi:10.2514/6.2019-3243.

[5] Drela, M., "TASOPT 2.00: transport aircraft system optimization—technical description," , 2010.

[6] Cavagna, L., Ricci, S., and Travaglini, L., "NeoCASS: an integrated tool for structural sizing, aeroelastic analysis and MDO at conceptual design level," *Progress in Aerospace Sciences*, Vol. 47, No. 8, 2011, pp. 621–635.

[7] Altus, S., and Kroo, I., "Concurrent wing design and flight-path optimization using optimizer-based decomposition," *7th AIAA/USAF/NASA/ISSMO Symposium on Multidisciplinary Analysis and Optimization*, 1998, p. 4920.

[8] Piperni, P., Abdo, M., and Kafyeke, F., "The development of a multi-disciplinary wing design method," Tech. rep., SAE Technical Paper, 2003.

[9] Piperni, P., Abdo, M., and Fafyeke, F., "The application of multi-disciplinary optimization technologies to the design of a business jet," *10th AIAA/ISSMO Multidisciplinary Analysis and Optimization Conference*, 2004, p. 4370.

[10] Piperni, P., Abdo, M., Kafyeke, F., and Isikveren, A. T., "Preliminary aerostructural optimization of a large business jet," *Journal of Aircraft*, Vol. 44, No. 5, 2007, pp. 1422–1438.

[11] Jasa, J. P., Hwang, J. T., and Martins, J. R. R. A., "Open-source coupled aerostructural optimization using Python," *Structural and Multidisciplinary Optimization*, Vol. 57, No. 4, 2018, pp. 1815–1827. doi:10.1007/s00158-018-1912-8.

[12] Hwang, J., and Martins, J., "GeoMACH: geometry-centric MDAO of aircraft configurations with high fidelity," *12th AIAA Aviation Technology, Integration, and Operations (ATIO) Conference and 14th AIAA/ISSMO Multidisciplinary Analysis and Optimization Conference*, 2012, p. 5605.

[13] Kenway, G. K., and Martins, J. R., "Multipoint high-fidelity aerostructural optimization of a transport aircraft configuration," *Journal of Aircraft*, Vol. 51, No. 1, 2014, pp. 144–160.

[14] Kennedy, G. J., and Martins, J. R., "A parallel finite-element framework for large-scale gradient-based design optimization of high-performance structures," *Finite Elements in Analysis and Design*, Vol. 87, 2014, pp. 56–73.

[15] Lambe, A. B., and Martins, J. R. R. A., "Extensions to the design structure matrix for the description of multidisciplinary design, analysis, and optimization processes," *Structural and Multidisciplinary Optimization*, Vol. 46, No. 2, 2012, pp. 273–284. doi:10.1007/s00158-012-0763-y, 968mw Times Cited:61 Cited References Count:33.

[16] Corman, J. A., Weston, N., Friedland, C., Mavris, D. N., and Laughlin, T. W., "A parametric multi-fidelity approach to conceptual airframe design," *2018 AIAA Modeling and Simulation Technologies Conference*, 2018, p. 1930.

[17] Chakraborty, I., and Mavris, D. N., "Heuristic Definition, Evaluation, and Impact Decomposition of Aircraft Subsystem Architectures," *16th AIAA Aviation Technology, Integration, and Operations Conference*, American Institute of Aeronautics and Astronautics, 2016. doi:10.2514/6.2016-3144.

[18] McCullers, L., *Flight Optimization System, Release 8.11, User's Guide*, NASA Langley Research Center, Hampton, VA 23681-0001, Oct. 2009.

[19] Drela, M., and Youngren, H., *AVL 3.36 User Primer*, MIT, Feb. 2017.

[20] Wells, D. P., Horvath, B. L., and McCullers, L. A., "The Flight Optimization System Weights Estimation Method," Tech. rep., 2017.

[21] Roskam, D. J., *Airplane Design Part V : Component Weight Estimation*, Design, Analysis and Research Corporation (DARcorporation), 2017.

[22] Chakraborty, I., "Subsystem architecture sizing and analysis for aircraft conceptual design," Ph.D. thesis, Georgia Institute of Technology, 2015.

[23] Chakraborty, I., and Mavris, D. N., "Integrated Assessment of Aircraft and Novel Subsystem Architectures in Early Design," *Journal of Aircraft*, Vol. 54, No. 4, 2017, pp. 1268–1282. doi:10.2514/1.c033976.

[24] *Code of Federal Regulations, Title 14, Federal Aviation Regulations, Part 25 - Airworthiness Standards: Transport Category Airplanes*, Federal Aviation Administration, 2019. URL https://www.ecfr.gov/cgi-bin/text-idx?SID=01562231188568 0c5924c66bdbc66b2c&mc=true&node=pt14.1.25&rgn=div5.

[25] Goron, G., Duca, R., Sarojini, D., Shah, S., Chakraborty, I., Briceno, S. I., and Mavris, D. N., "A Simulation-Based Framework for Structural Loads Assessment during Dynamic Maneuvers," *17th AIAA Aviation Technology, Integration, and Operations Conference*, 2017, p. 3767.

[26] Duca, R., Sarojini, D., Bloemer, S., Chakraborty, I., Briceno, S. I., and Mavris, D. N., "Effects of Epistemic Uncertainty on Empennage Loads During Dynamic Maneuvers," *2018 AIAA Aerospace Sciences Meeting*, 2018, p. 0767.

[27] Sarojini, D., Duca, R., Solano, H. D., Chakraborty, I., Briceno, S. I., and Mavris, D. N., "Framework to Assess Effects of Structural Flexibility on Dynamic Loads Developed in Maneuvering Aircraft," *2018 Aviation Technology, Integration, and Operations Conference*, 2018, p. 4147.

[28] Corman, J. A., Sarojini, D., Gharbi, A., and Mavris, D. N., "Estimating jig shape for an aircraft wing determined through aerodynamic shape optimization with rigid body assumptions," *AIAA Scitech 2019 Forum*, 2019, p. 0418.

[29] Cai, Y., Rajaram, D., and Mavris, D. N., "Multi-mission Multi-objective Optimization in Commercial Aircraft Conceptual Design," *AIAA Aviation 2019 Forum*, American Institute of Aeronautics and Astronautics, 2019. doi:10.2514/6.2019-3577.

[30] *Advisory Circular AC 25-7D Flight Test Guide for Certification of Transport Category Airplanes*, Federal Aviation Administration, May 2018. URL https://www.faa.gov/documentLibrary/media/Advisory_Circular/AC_25-7D.pdf.

[31] Xie, J., Chakraborty, I., Briceno, S. I., and Mavris, D. N., "Development of A Certification Module for Early Aircraft Design," *AIAA Aviation 2019 Forum*, American Institute of Aeronautics and Astronautics, 2019. doi:10.2514/6.2019-3576.

[32] *777-200/200ER/-300 Airplane Characteristics for Airport Planning*, Boeing Commercial Airplanes, revision e ed., May 2015.

[33] Mavris, D. N., and Schutte, J. S., "Application of deterministic and probabilistic system design methods and enhancements of conceptual design tools for era project," 2016.

[34] Wang, S., Tomovic, M., and Liu, H., *Commercial Aircraft Hydraulic Systems*, Elsevier, 2016. doi:10.1016/c2013-0-09774-5.

[35] Yeh, Y., "Design considerations in Boeing 777 fly-by-wire computers," *Proceedings Third IEEE International High-Assurance Systems Engineering Symposium (Cat. No.98EX231)*, IEEE Comput. Soc, 1998. doi:10.1109/hase.1998.731596.

[36] "Air Carrier Statistics (Form 41 Traffic)- U.S. Carriers," Online, Oct. 2018. URL https://www.transtats.bts.gov/tables.asp?db_id=110&DB_Name=.

[37] Liem, R. P., Kenway, G. K. W., and Martins, J. R. R. A., "Multimission Aircraft Fuel-Burn Minimization via Multipoint Aerostructural Optimization," *AIAA Journal*, Vol. 53, No. 1, 2015, pp. 104–122. doi:10.2514/1.j052940.

[38] Moorhouse, D., and Woodcock, R., "Us military specification mil-f-8785c," *US Department of Defense*, 1980.

[39] Mavris, D. N., Bandte, O., and DeLaurentis, D. A., "Robust design simulation: a probabilistic approach to multidisciplinary design," *Journal of Aircraft*, Vol. 36, No. 1, 1999, pp. 298–307.

[40] Bendarkar, M. V., Chakraborty, I., Garcia, E., and Mavris, D. N., "Rapid Assessment of Power Requirements and Optimization of Thermal Ice Protection Systems," *AIAA Aviation Technology, Integration, and Operations Conference*, Atlanta, GA, 2018. doi:10.2514/6.2018-4136.

[41] Bendarkar, M. V., Rajaram, D., Cai, Y., Briceno, S. I., and Mavris, D. N., "Evaluating Optimal Paths for Aircraft Subsystem Electrification in Early Design," *AIAA Aviation 2019 Forum*, Dallas, TX, 2019. doi:10.2514/6.2019-2802.

[42] Sarojini, D., Gupta, M., Hodges, D. H., and Mavris, D. N., "An Efficient Method to Dimensionally Reduce Aperiodic Inhomogeneous 3-D Structures to 1-D Beam-Like Structures," *AIAA Scitech 2020 Forum*, 2020, p. 0272.

[43] Gupta, M., Sarojini, D., Shah, A., and Hodges, D. H., "Beam Theory for Asymptotic Analysis of Aperiodic and Inhomogeneous Structures," *AIAA Journal*, Vol. 57, No. 10, 2019, pp. 4155–4168.

[44] Sarojini, D., Rajaram, D., Solano, D., and Mavris, D. N., "Adjoint-Based Structural Optimization for Beam-Like Structures Subjected to Dynamic Loads," *AIAA Scitech 2020 Forum*, 2020, p. 0273.